magnetochemistry

MDPI

Article

Magnetized Heavy Ion-Acoustic Wave Envelopes: Hamiltonian Phase-Space Dynamics, Modulational Instability, and Akhmediev Breathers with a Kappa-Cairns Distribution

Abdullah Khan [1,*], Yakup Yildirim [2], Wasem Aljuaid [3], Yanfang Ji [1], Guangrui Yao [1] and Taha Radwan [4,*]

[1] Department of Physics, Qilu Institute of Technology, Jinan 250200, China
[2] Department of Computer Engineering, Biruni University, Istanbul 34010, Turkey
[3] Department of Physics, Faculty of Science, Islamic University of Madinah, Madinah 42351, Saudi Arabia
[4] Department of Management Information Systems, College of Business and Economics, Qassim University, Buraydah 51452, Saudi Arabia
* Correspondence: abdullah@qlit.edu.cn (A.K.); t.radwan@qu.edu.sa (T.R.)

Abstract

This work presents a unified mathematical framework for investigating the influence of an external magnetic field on Hamiltonian phase-space dynamics, Akhmediev breather solitons, and modulational instability in heavy ion-acoustic waves propagating through a magnetized four-component non-Maxwellian plasma. Using the multiscale perturbation method, a nonlinear Schrödinger equation is obtained to describe the evolution of nonlinear wave envelopes. A traveling-wave reduction transforms this equation into a planar Hamiltonian system, linking its phase-space geometry to analytical solitary-wave solutions. The resulting phase portraits exhibit periodic, superperiodic, and homoclinic trajectories, with the homoclinic orbits yielding paired solitary-wave envelope solutions related by polarity reversal. Furthermore, the results demonstrate that the plasma system supports both bright and dark solitons under the influence of combined kappa(κ)-Cairns statistics, depending on the balance between dispersion and nonlinearity. The influence of heavy ion-acoustic plasma parameters, including electron superthermality, magnetic field strength, positron concentration, charged-weighted ion-mass ratio, and temperature ratio on the instability threshold, growth rate, and spectral bandwidth is systematically examined. Exact Akhmediev breather solutions are constructed in the modulationally unstable regime using the Darboux transformation. The modulation frequency governs their spatial periodicity and localization during envelope evolution, while the magnetic field modifies their spatial period in a manner that depends on the carrier wavenumber. These findings elucidate how magnetic-field strength and non-Maxwellian particle statistics jointly influence nonlinear envelope dynamics. This study establishes a unified connection between Hamiltonian phase-space geometry, sign-reversal symmetric solitary waves, modulational instability spectra, and nonlinear breather excitations, providing a mathematical description of magnetic field effects on nonlinear wave dynamics in non-Maxwellian plasmas relevant to space and laboratory environments.

Keywords: Hamiltonian; traveling wave solution; envelope solitons; wave stability; Darboux transformation

Check for updates

Academic Editor: Oluwole D. Makinde

Received: 14 October 2026
Revised: 2 November 2026
Accepted: 5 November 2026
Published: 9 November 2026

Copyright: © 2026 by the authors. Licensee MDPI, Basel, Switzerland. This article is an open access article distributed under the terms and conditions of the Creative Commons Attribution (CC BY) license.

1. Introduction

Multicomponent plasmas, particularly those comprising electrons and multiple ion species, are widely encountered in space and laboratory environments and play a funda-

mental role in collective plasma dynamics. Among the various multicomponent configurations, electron–positron–ion (EPI) [1,2] plasmas represent a specialized class of considerable theoretical interest, particularly in high-energy astrophysical environments and laser-produced pair plasmas [3–9]. The inclusion of positrons introduces additional charge-balance and nonlinear coupling effects that can significantly modify the dispersion, modulational stability, and nonlinear evolution of ion-acoustic wave packets. The coexistence of electrons, ions, and positrons substantially modifies the propagation characteristics of electrostatic disturbances compared with conventional ion–electron plasmas [10–12]. Among various nonlinear electrostatic modes, the dust-acoustic and ion-acoustic waves (IAWs) are the most fundamental low-frequency collective oscillations, where the ion inertia provides the restoring mechanism while the electron and positron's thermal pressure acts as the restoring force. Physicists have employed such waves to examine various nonlinear electrostatic structures in different plasma systems, notably the envelope solitons and the rogue waves [13]. The presence of positrons introduces additional degrees of freedom and significantly alters the IAW's linear and nonlinear features. The impact of an external field strength further modifies the dispersive properties of IAWs and plays a crucial role in determining the stability and localization characteristics of nonlinear wave packets [14]. Understanding the propagation dynamics of IAWs in magnetized EPI plasmas is of considerable importance for interpreting nonlinear processes occurring in both space and laboratory plasma configurations [6,9,10]. These earlier investigations have demonstrated that magnetized EPI plasmas support a rich variety of nonlinear excitations, namely, solitary waves, envelope solitons, and rogue waves.

For studying the modulational instability (MI) of IAWs and the associated envelope solitons [15], breathers [16], and rogue wave dynamics [17] in dispersive plasma media, the nonlinear Schrödinger equation (NLSE) is assumed as one of the most powerful theoretical frameworks. Derived through the reductive perturbation approach, the NLSE describes the slow spatiotemporal evolution of weakly nonlinear wave packets by balancing nonlinear self-interaction with wave dispersion [16,18]. They have shown that the relative signs of the dispersive and nonlinear coefficients determine the stability of the carrier wave and the emergence of bright or dark envelope structures. The NLSE has been extensively employed to investigate MI and rogue-wave dynamics in EPI plasmas containing Maxwellian, nonthermal, superthermal, and nonextensive particle populations and serve as a fundamental analytical tool for understanding nonlinear wave dynamics in realistic plasma environments [2,14,19]. Since MI represents the fundamental mechanism through which a uniform carrier wave becomes unstable against long-wavelength perturbations, it plays a pivotal role in the formation of envelope solitons, breathers, and rogue waves. These wave phenomena have been thoroughly studied in plasma physics, communication systems, nonlinear optics, superfluid helium, Bose–Einstein condensates, hydrodynamics, acoustic-gravity wave's propagation in the atmosphere, and atmospheric physics [20–27]. In plasma systems, the rogue waves are highly localized structures that emerge through energy localization and may attain amplitudes several times larger than surrounding background waves before disappearing rapidly. Beyond plasma physics, localized nonlinear structures and soliton-like excitations have gained increasing attention for their applications in emerging technologies. Recent studies have demonstrated that cavitation bubble collapse can generate powerful mechanical impulses for microbot propulsion and microscale actuation [28]. Similarly, bound-state solitons in ultrafast fiber lasers offer new possibilities for controlling optical pulse dynamics and advancing photonic technologies [29]. These developments highlight the importance of understanding nonlinear wave localization, stability, and evolution across different physical systems. In this context,

investigating plasma envelope solitons and breather dynamics provides valuable insights into the broader behavior of localized nonlinear structures.

The velocity distribution of plasma particles deviates substantially from the classical Maxwellian distribution with high-energy particles experiencing collisions much less frequently than their low-energy counterparts. Since the mean free path of energetic particles scales approximately as v^4, where v denotes the particle velocity, these particles experience fewer collisions and consequently undergo insufficient collisional relaxation to attain thermal equilibrium. As a result, the particle population exhibits non-Maxwellian characteristics, with an enhanced high-energy tail superimposed on an approximately Maxwellian low-energy core [30]. These non-Maxwellian distributions arise because the collisional relaxation times of energetic particles are sufficiently long to prevent complete thermalization, allowing nonequilibrium particle populations and enhanced suprathermal tails to persist in weakly collisional plasma environments [31]. Extensive spacecraft observations have confirmed the ubiquitous presence of highly energetic electrons in space plasmas, resulting in velocity distributions characterized by long high-energy tails that deviate substantially from the Maxwellian form [32,33]. These suprathermal electron populations are usually represented by the Kappa distribution, which predicts a significantly higher number of energetic particles than that of the Maxwellian distribution, while simultaneously preserving an enhanced particle density near the low-velocity region. The Kappa distribution was first developed by Olbert during the analysis of plasma measurements from the IMP-1 mission [34], and was subsequently adopted by Vasyliunas in his pioneering studies of space plasmas [35]. Since then, it has become the most extensively investigated distribution function for modeling nonequilibrium plasmas in both theoretical and observational studies [36–40].

In contrast, the Cairn's nonthermal distribution provides an alternative description of energetic electrons by incorporating a nonthermal parameter (β_e), which governs the deviation from thermal equilibrium. As β_e increases, the distribution develops dramatic symmetric wings about the zero-velocity point $(v = 0)$, indicating a progressive enhancement of energetic particles in the finite region of phase space. Unlike the κ-distribution, which primarily modifies the high-energy tail, the Cairns distribution introduces a characteristic flattening of the velocity profile at intermediate particle energies while maintaining the Maxwellian distribution as the background state [32]. Owing to its ability to capture moderate-energy nonthermal populations, the Cairns distribution has been successfully applied to investigate a wide range of linear and nonlinear wave phenomena in diverse plasma environments [41–44]. To incorporate the combined influence of suprathermal and nonthermal particle populations more realistically, Aoutou et al. [45] proposed a generalized κ-Cairns velocity distribution, which unifies fundamental characteristics of both distributions into a single theoretical framework for modeling complex plasma systems.

In different plasma configurations, IAWs have been extensively investigated because of their fundamental role in nonlinear wave dynamics. Using a three-component magnetized EPI plasma model, Mahmood et al. [46] examined the nonlinear evolution of IAWs and demonstrated that the amplitude of the resulting solitary waves is strongly influenced by the positron concentration, angle of wave propagation, and Mach number. In a related study, the oblique propagation of electrostatic waves was explored in a magnetized EPI plasma by Alinejad et al. [47], in which the electrons are described by the κ-distribution that highlights the significant influence of suprathermal electrons on wave propagation features. Chowdhury et al. [10] investigated the HIA rogue waves in an unmagnetized electron–positron multi-ion plasma, elucidating the key nonlinear characteristics, namely, the MI threshold, instability growth rate, and the amplitude of the extreme rogue waves. They are dramatically affected by the ion mass, electron temperature, and the nonex-

tensivity parameter (q). Likewise, Bacha et al. [48] analyzed the IAWs of a magnetized plasma in the Earth's magnetosphere. Although considerable progress has been made in understanding nonlinear ion-acoustic waves in magnetized electron–positron–ion plasmas, several important aspects remain insufficiently explored. Our previous studies [16,18,49] investigated modulational instability (MI), Akhmediev breathers, and rogue-wave dynamics in electronegative, ion-acoustic, and dual-polarity dusty plasmas using different non-Maxwellian statistical models. However, the combined influence of external magnetic fields, κ-Cairns-distributed electrons, and nonextensive positrons on the nonlinear dynamics of heavy ion-acoustic waves has received relatively limited attention. In particular, how magnetization affects Hamiltonian phase-space structures, modulational stability, and Akhmediev breather evolution within a unified framework remains inadequately understood. To address these research gaps, the present study develops a distinct magnetized four-component heavy ion-acoustic plasma model that systematically connects Hamiltonian phase-space dynamics, compressive and rarefactive solitary waves, modulational instability, and exact Akhmediev breather solutions. This unified approach provides deeper insight into the coupled effects of magnetization and non-Maxwellian particle distributions on nonlinear wave propagation, stability transitions, and localized energy concentration in magnetized space and laboratory plasma environments.

Therefore, motivated by these considerations and recent developments in magnetized heavy ion-acoustic wave (HIAW) plasmas, the present work explores the nonlinear propagation of ion-acoustic waves in a magnetized HIAW plasma comprising κ-Cairns-distributed electrons and nonextensive positrons. The simultaneous inclusion of superthermal electrons and nonextensive positrons introduces additional nonlinear coupling mechanisms that significantly influence the wave dynamics. The principal novelty of this work lies in establishing a unified framework that connects Hamiltonian phase-space dynamics, modulational instability, and Akhmediev breather excitations in the considered magnetized plasma configuration. In contrast to conventional studies treating these phenomena separately, we systematically investigate how magnetic-field variations influence phase-space trajectories, solitary-wave structures, disconnected stability regions, instability growth rates, and breather spatial periodicity. To accomplish this, the reductive perturbation method is employed to derive the nonlinear Schrödinger equation (NLSE), providing the basis for examining modulational stability and associated nonlinear envelope excitations. The combined effects of the nonextensive and nonthermal parameters, magnetic-field strength, positron concentration, and temperature ratio are systematically analyzed, providing new insights into localized envelope structures and extreme wave events with potential relevance to laboratory and astrophysical plasma environments.

The remainder of this paper is organized as follows. Section 2 presents the governing fluid equations for the magnetized EPI plasma and combined κ-Cairns and nonextensive distribution functions. In Section 3, we use the reductive perturbation method to derive the NLSE governing the evolution of IAW envelopes. In Section 4, we examine the dynamical system of magnetized HIAWs and compressive and rarefactive soliatry waves. Section 5 discusses the MI criterion and its growth rate under different plasma parameters. The formation and characteristics of breather structures are presented in Section 6. Finally, the conclusions and physical implications of the current investigation are summarized in Section 7.

2. Plasma Model with Combined κ-Cairns Statistics

2.1. Plasma Model

We consider the HIAW propagation in a collisionless four-component magnetized plasma composed of inertial light positive ions (mass m_1 and charge Z_1e), inertial heavy

negative ions (mass m_2 and charge $-Z_2e$), inertialess κ-Cairns-distributed electrons (mass m_e and charge $-e$), and inertialess positrons (mass m_p and charge $+e$). Under equilibrium conditions, the overall charge neutrality of the plasma system is maintained through the relation $Z_1n_{10} + n_{p0} = Z_2n_{20} + n_{e0}$, where n_{s0} ($s = e, p, 1, 2$) denotes the equilibrium number density of electrons, positrons, light positive ions, and heavy negative ions, respectively. Throughout the present analysis, the external static magnetic field is considered to be directed along the $\hat{z}$-axis, i.e., $\mathbf{B}_0 = B_0\hat{z}$, while the carrier wave propagates along the x-direction with wave vector $\mathbf{k} = k\hat{x}$. Consequently, all physical quantities are assumed to be uniform along the transverse directions, implying that their spatial gradients with respect to the y- and z-coordinates vanish. Under these assumptions, the nonlinear evolution of HIAWs in the magnetized plasma system is governed by the following set of normalized fluid equations:

$$\frac{\partial n_1}{\partial t} + \frac{\partial}{\partial x}(n_1u_{1x}) = 0, \tag{1}$$

$$\frac{\partial u_{1x}}{\partial t} + u_{1x}\frac{\partial u_{1x}}{\partial x} = -\frac{\partial \Psi}{\partial x} + \omega_{c1}u_{1y}, \tag{2}$$

$$\frac{\partial u_{1y}}{\partial t} + u_{1x}\frac{\partial u_{1y}}{\partial x} = -\omega_{c1}u_{1x}, \tag{3}$$

$$\frac{\partial u_{1z}}{\partial t} + u_{1x}\frac{\partial u_{1z}}{\partial x} = 0, \tag{4}$$

$$\frac{\partial n_2}{\partial t} + \frac{\partial}{\partial x}(n_2u_{2x}) = 0, \tag{5}$$

$$\frac{\partial u_{2x}}{\partial t} + u_{2x}\frac{\partial u_{2x}}{\partial x} = -\alpha\frac{\partial \Psi}{\partial x} - \alpha\omega_{c1}u_{2y}, \tag{6}$$

$$\frac{\partial u_{2y}}{\partial t} + u_{2x}\frac{\partial u_{2y}}{\partial x} = \alpha\omega_{c1}u_{2x}, \tag{7}$$

$$\frac{\partial u_{2z}}{\partial t} + u_{2x}\frac{\partial u_{2z}}{\partial x} = 0, \tag{8}$$

$$\frac{\partial^2 \Psi}{\partial x^2} = \mu_e n_e - \mu_p n_p - n_1 + (1 - \mu_e + \mu_p)n_2. \tag{9}$$

where the normalized parameters are $\alpha = Z_2m_1/Z_1m_2$ (charged-weighted mass ratio), $\mu_e = n_{e0}/n_{10}$ (electron density ratio), $\mu_p = n_{p0}/n_{10}$ (positron density ratio) and $\omega_{c1} = \Omega_1/\omega_{p1}$, and $\lambda = 1 - \mu_e + \mu_p$. In the above model equations, the ion gyrofrequency is defined as $\Omega_1 = |Z_1e|B_0/m_1$, where B_0 denotes the magnitude of the external magnetic field. The normalized quantities n_1 and n_2 represent the number densities of the light positive and heavy negative ions, respectively. They are scaled by their corresponding equilibrium values n_{10} and n_{20}. Likewise, the fluid velocities u_1 and u_2 correspond to the light positive and heavy negative ion species and are normalized by the characteristic ion-acoustic speed $C_{s1} = \sqrt{Z_1k_BT_e/m_1}$. Moreover, the electrostatic potential Ψ is normalized by the electron thermal potential k_BT_e/e, where e is the elementary charge and k_B is the Boltzmann constant. Furthermore, m_1 and m_2 denote the masses of the light positive and heavy negative ions, respectively, whereas T_e and T_p represent the electron and positron temperatures. The temporal variable t is normalized by the inverse of the positive-ion plasma frequency, $\omega_{p1}^{-1} = (m_1/4\pi Z_1^2e^2n_{10})^{1/2}$, while the spatial coordinate is scaled by the corresponding Debye length, $\lambda_{D1} = (k_BT_e/4\pi Z_1e^2n_{10})^{1/2}$.

It is well established that positive- and negative-ion plasmas naturally occur in numerous space and laboratory plasma systems. Representative examples include the (H^+, H^-) and (H^+, O_2^-) plasma systems observed in the D- and F-regions of the Earth's ionosphere, as well as the (Ar^+, F^-) plasma produced under laboratory conditions. For these plasma compositions, the ion mass ratio (m_1/m_2) takes approximate values of 1, 0.0625, and 2.1 for the (H^+, H^-), (H^+, O^-), and (Ar^+, F^-) systems, respectively [17].

2.2. Combined κ-Cairns Statistics

The generalized κ-distribution is used in space plasma studies to describe the one-dimensional (1D) electron velocity distribution in non-Maxwellian plasmas. It effectively accounts for superthermal particle populations [50–52]. Nonthermal deviations are often observed in many laboratory and astrophysical plasmas, which cannot be effectively elucidated by traditional κ-distribution alone. To solve this constraint, Debnath et al. [37] modeled the generalized κ-Cairns distribution, which combines the κ-distribution with the Cairns model to simultaneously integrate the superthermal and nonthermal features of the plasma species. The corresponding 1D velocity distribution function is expressed as

$$f_{\kappa e}\left(v_z^2\right) = \frac{n_{e0}}{\left(\pi\kappa\theta^2\right)^{1/2}} \frac{\Gamma(\kappa)}{\Gamma\left(\kappa - \frac{1}{2}\right)} \left(1 + \frac{v_z^2}{\kappa\theta^2}\right)^{-\kappa}, \tag{10}$$

where θ represents the effective electron thermal velocity that measures the thermal population of the electron population in equilibrium state and is expressed as

$$\theta = \sqrt{\frac{2\kappa - 3}{\kappa} \frac{K_B T_e}{m_e}}. \tag{11}$$

The parameters k_B, n_{e0}, and m_e in Equations (10) and (11) denote the Boltzmann constant, equilibrium electron density, and electron mass, respectively. Moreover, $\Gamma(\kappa)$ is the Gamma function, and the quantities T_e and v_z are the mean electron temperature and electron velocity along the propagation direction, respectively.

The κ-distribution function is a single-peaked, symmetric, long-tailed profile centered at $v_z = 0$, and effectively depicts superthermal electrons. Localized populations of fast and energetic electrons close to the core of the velocity space are not explained by this Maxwellian distribution. Therefore, inspired by observations of auroral electric field structures from the *Freja* satellite [53], Cairns et al. [32] developed a non-Maxwellian distribution that simultaneously takes into account a localized energetic electron constituent and a thermal Maxwellian background. In contrast to the Maxwellian distribution, whose electron population peaks at $v_z = 0$, the Cairns distribution suggests a progressive depletion of electrons near the phase-space center with increasing nonthermality. The 1D Cairns velocity distribution can be written as [32]

$$f_C(v_z^2) = \frac{n_{e0}\left[1 + \alpha_e\left(\frac{v_z}{v_{te}}\right)^4\right]}{(1 + 3\alpha_e)\sqrt{2\pi}\, v_{te}} \exp\left(-\frac{v_z^2}{2v_{te}^2}\right), \tag{12}$$

where $v_{te} = \sqrt{\frac{k_B T_e}{m_e}}$, and $\alpha_e \geq 0$.

The generalized κ-Cairns velocity distribution function in this context can be expressed as follows:

$$f_{\kappa c}(v_z^2) = A n_{e0}\left[1 + \alpha_e\left(\frac{v_z}{v_{te}}\right)^4\right]\left(1 + \frac{v_z^2}{\kappa\theta^2}\right)^{-\kappa}, \tag{13}$$

where

$$A = \frac{1}{\sqrt{\pi\kappa\theta^2}} \frac{\Gamma(\kappa)}{\Gamma\left(\kappa - \frac{5}{2}\right)} \frac{1}{\kappa_1\kappa_2 + 3\alpha_e\kappa_1^2}, \tag{14}$$

with

$$\kappa_1 = \kappa - \frac{3}{2}, \qquad \kappa_2 = \kappa - \frac{5}{2}. \tag{15}$$

The physical nature of the generalized κ-Cairns distribution $f_{\kappa C}(v_z)$ as a function of velocity v_z can be quantified for various values of the nonthermal parameter α_e (or, alternatively, $\beta_e = 4\alpha_e/(1+3\alpha_e)$). This nonthermal parameter shows the fraction of energetic particles that are concentrated nearly to $v_z = 0$. When $\beta_e = 0$ (or $\alpha_e = 0$), the distribution becomes the κ-distribution. In contrast, as $\kappa \to \infty$, it gets closer to the nonthermal Cairns distribution. Its theoretical range is $0 \leq \beta_e < 4/3$ and β_e increases with α_e, although all values in this range are physically not valid [37]. Here, we consider $\int_{\infty}^{\infty} f_{\kappa C}(v_z^2) dv_z = 1$. The κ-distribution has a single peak at $v_z = 0$, which differs qualitatively from Cairns behavior. The threshold value β_{eT} and the normalized velocity are mathematically given as [37]:

$$\beta_{eT} = \frac{4}{3 + \dfrac{4(\kappa_1/\kappa)^2}{1-(2/\kappa)}}, \tag{16}$$

$$\frac{V}{v_{te}} = \sqrt{\frac{\dfrac{2\kappa_1}{\kappa} + 2\sqrt{1-\dfrac{2}{\kappa}}\sqrt{\dfrac{1}{\beta_{eT}} - \dfrac{1}{\beta_e}}}{1-\dfrac{2}{\kappa}}}. \tag{17}$$

This work aims to model a velocity distribution with more high-energy particles than kappa or Maxwell–Boltzmann distributions. Under the constraint $0 \leq \beta_e \leq \beta_{eT}$, the integrated κ-Cairns distribution describes a non-isothermal plasma and diverges notably from the conventional κ-distribution. The nonthermal parameter (β_e) in the Maxwellian limit $(\kappa \to \infty)$ is restricted to the range $0 \leq \beta_e \leq 4/7$. This range aligns with earlier findings by Verheest and Pillay [54], who confirmed the effective range of β_e lies within these constraints. Under such constraint, the wave phase speed reduces to $V = v_{te}\sqrt{2+\sqrt{7-4(\beta_e)^{-1}}}$, consistent with results from Debnath et al. [37]. Therefore, β_e for the κ-Cairns distribution is bounded by $0 \leq \beta \leq \beta_{eT}$. In the framework of the generalized κ-Cairns distribution described by Equation (13), the steady-state solution of the electron Vlasov–Boltzmann equation is formulated as follows:

$$f_e(v_z, \Psi) = f_{\kappa C}\left(v_z^2 - \frac{2e\Psi}{m_e}\right). \tag{18}$$

Accordingly, the electron number density formulated by the generalized κ-Cairns distribution can be expressed as follows:

$$n_{e\kappa C} = \int_{-\infty}^{\infty} f_e(v_z, \Psi)\, dv_z. \tag{19}$$

It is important to emphasize that the generalized κ-Cairns distribution employed in this study represents an effective quasi-stationary description of the background electron population rather than an exact time-dependent kinetic equilibrium [32,37,55,56]. This approximation is applicable when the characteristic timescale of weakly nonlinear envelope evolution is sufficiently shorter than that of substantial kinetic relaxation or redistribution of energetic electrons. Under such conditions, the nonthermal and suprathermal characteristics of the electron population may be treated as approximately preserved during ion-acoustic wave propagation [37,55,56]. Nevertheless, strong temporal variations, particle acceleration, and kinetic relaxation may modify the underlying velocity distribution. Incorporating these effects through a self-consistent time-dependent kinetic framework represents an important direction for future investigation.

Following the procedure by Debnath et al. [37], the normalized electron density from Cairn-Kappa distribution function is derived as

$$n_{e\kappa C} = \left(1 - \beta_{e1}^{(\kappa)}\Psi + \beta_{e2}^{(\kappa)}\Psi^2\right)\left(1 - \frac{\Psi}{\kappa_1}\right)^{-\kappa+\frac{1}{2}}. \tag{20}$$

where the parameters of the distribution function are specified as:

$$\beta_{e1}^{(\kappa)} = \beta_e^{(\kappa)}\left(1 + \frac{3}{2\kappa_2}\right), \qquad \beta_{e2}^{(\kappa)} = \beta_e^{(\kappa)}\left(1 + \frac{1}{\kappa_1} + \frac{3}{4\kappa_1\kappa_2}\right),$$

$$\beta_e^{(\kappa)} = \frac{4\alpha_e}{1 + 3\alpha_e\frac{\kappa_1}{\kappa_2}}, \qquad \kappa_1 = \kappa - \frac{3}{2}, \qquad \kappa_2 = \kappa - \frac{5}{2}.$$

The electron nonthermal parameter β_e in the generalized κ-Cairns model is defined as $\alpha_e/(1+3\alpha_e)$, while κ represents the suprathermal index governing the distribution of high-energy tail particles [37]. Debnath and Bandyopadhyay [37] explained that this distribution is inherently non-isothermal and converges to the standard κ-distribution when β_e satisfies the following inequality:

$$0 \le \beta_e \le \beta_{eT}, \qquad \text{where} \qquad \beta_{eT} = \frac{4}{3 + \frac{4(\kappa_1/\kappa)^2}{1 - (2/\kappa)}}. \tag{21}$$

The positron number density follow the nonextensive statistic and can be written as [14]

$$n_p = (1 - (q-1)\sigma\Psi)^{\frac{3q-1}{2q-2}}. \tag{22}$$

This work employs the combined κ-Cairns distribution to analyze the behavior of magnetized HIAWs in plasma systems that can be described by nonthermal features in the context of the collisionless four-component magnetized plasma model and Poisson's equation. The magnetized HIAWs, which exhibit small amplitudes, will be examined using Equations (1)–(9). The Poisson's equation takes on the following form when the extended form of n_e and n_p from Equation (20) and Equation (22) is substituted into Equation (9):

$$\frac{\partial^2\Psi}{\partial x^2} = \mu_e - \mu_p - n_1 + \lambda n_2 + T_1\Psi + T_2\Psi^2 + T_3\Psi^3, \tag{23}$$

where $\lambda = 1 - \mu_e + \mu_p$ and the coefficients T_1, T_2, and T_3 are derived as

$$T_1 = \mu_e\left(\frac{\kappa - \frac{1}{2}}{\kappa_1} - \beta_{e1}^{(\kappa)}\right) + \mu_p\sigma\left(\frac{q+1}{2}\right), \tag{24}$$

$$T_2 = \mu_e\left[\frac{\kappa^2 - \frac{1}{4}}{2\kappa_1^2} - \beta_{e1}^{(\kappa)}\left(\frac{\kappa - \frac{1}{2}}{\kappa_1}\right) + \beta_{e2}^{(\kappa)}\right] - \mu_p\sigma^2\left[\frac{(q+1)(3-q)}{8}\right], \tag{25}$$

$$T_3 = \mu_e\left[\frac{\left(\kappa^2 - \frac{1}{4}\right)\left(\kappa + \frac{3}{2}\right)}{6\kappa_1^3} - \beta_{e1}^{(\kappa)}\left(\frac{\kappa^2 - \frac{1}{4}}{2\kappa_1^2}\right) + \beta_{e2}^{(\kappa)}\left(\frac{\kappa - \frac{1}{2}}{\kappa_1}\right)\right] + \mu_p\sigma^3\left[\frac{(q+1)(3-q)(5-3q)}{48}\right]. \tag{26}$$

3. Derivation of the Nonlinear Evolution Equation

To examine the modulational stability characteristics of magnetized HIAW packets and the subsequent formation of nonlinear localized structures, we use the multiscale reductive perturbation method, which has proven to be a powerful analytical framework for deriving the NLSE and investigating rogue wave dynamics in dispersive plasma media [57].

This method enables the systematic treatment of weakly nonlinear wave modulation by introducing multiple spatial and temporal scales. Following the standard perturbation procedure, the independent fast variables x and t are transformed into the stretched coordinates as

$$\xi = \epsilon(x - v_g t), \qquad \tau = \epsilon^2 t, \tag{27}$$

where ϵ $(0 < \epsilon < 1)$ denotes a small dimensionless perturbation parameter characterizing the smallness of the wave amplitude, and v_g represents the group velocity associated with the slowly varying wave envelope. To investigate the nonlinear evolution of the carrier wave, the dependent variables, namely, the light positive ion number density $n_1(x,t)$, heavy negative ion number density $n_2(x,t)$, ion fluid velocity components $u_{1x}(x,t)$, $u_{1y}(x,t)$, $u_{1z}(x,t)$, $u_{2x}(x,t)$, $u_{2y}(x,t)$, $u_{2z}(x,t)$, and the electrostatic potential $\Psi(x,t)$, are expressed in terms of the small parameter ϵ as

$$F(x,t) = F_0 + \sum_{l=-\infty}^{\infty} \left(\sum_{m=1}^{\infty} \epsilon^{(m)} F_l^{(m)}(\xi,\tau) e^{il(kx+\omega t)} \right), \tag{28}$$

where $F(x,t)$ corresponds to the physical quantities describing the plasma dynamics with F_0 their unperturbed equilibrium component, and

$$F_l^{(m)} = \left[n_{1l}^{(m)}, n_{2l}^{(m)}, u_{1xl}^{(m)}, u_{1yl}^{(m)}, u_{1zl}^{(m)}, u_{2xl}^{(m)}, u_{2yl}^{(m)}, u_{2zl}^{(m)}, \Psi_l^{(m)} \right]^T, \qquad F_0^l = [1, 1, 0, 0, 0, 0, 0, 0, 0]^T. \tag{29}$$

In the above formulation, k and ω denote the real-valued carrier wave number and angular frequency of the fundamental wave, respectively. Since the physical quantities represented by $F_l^{(m)}$ must remain real, the harmonic amplitudes are required to satisfy the Hermitian symmetry condition $F_{-l}^{(m)} = \left(F_l^{(m)}\right)^\star$, where the superscript * indicates the complex conjugate. This condition guarantees the reality of the perturbed plasma variables and ensures the physical consistency of the harmonic expansion. Furthermore, the differential operators appearing in the governing equations are transformed according to the stretched coordinates and are expressed as follows:

$$\frac{\partial}{\partial t} \to \frac{\partial}{\partial t_0} - \epsilon v_g \frac{\partial}{\partial \xi} + \epsilon^2 \frac{\partial}{\partial \tau}, \qquad \frac{\partial}{\partial x} \to \frac{\partial}{\partial x_0} + \epsilon \frac{\partial}{\partial \xi} \tag{30}$$

Here, $x_0 = x$ and $t_0 = t$ denote thespatial and temporal scales associated with carrier-wave oscillations, whereas $\xi = \epsilon(x - v_g t)$ and $\tau = \epsilon^2 t$ describe the slow spatiotemporal evolution of the wave envelope. The differential operators are obtained by applying the chain rule while treating the fast and slow coordinates as independent variables within the multiscale expansion. Substituting the multiscale perturbation expansions of Equation (28) and the stretched variables introduced in Equation (30) into the normalized fluid Equations (1)–(8) together with Poisson's Equation (23), and then separating terms according to successive powers of the smallness parameter ϵ, leads to a sequence of coupled equations at different perturbation orders. At the leading order of approximation ($m = 1$), corresponding to the first harmonic component ($l = 1$), the following relations are obtained:

$$
\begin{aligned}
iku_{11x}^{(1)} - i\omega n_{11}^{(1)} &= 0,\\
\omega_{c1} u_{11x}^{(1)} - i\omega u_{11y}^{(1)} &= 0,\\
-\omega_{c1} u_{11y}^{(1)} + ik\Psi_1^{(1)} - i\omega u_{11x}^{(1)} &= 0,\\
-i\omega n_{21}^{(1)} + iku_{21x}^{(1)} &= 0,\\
-ik\alpha\Psi_1^{(1)} + \alpha\omega_{c1} u_{21y}^{(1)} - i\omega u_{21x}^{(1)} &= 0,\\
-i\omega u_{21y}^{(1)} - \alpha\omega_{c1} u_{21x}^{(1)} &= 0,\\
-i\omega u_{11z}^{(1)} &= 0,\\
-i\omega u_{21z}^{(1)} &= 0,\\
-k^2\Psi_1^{(1)} - T_1\Psi_1^{(1)} - \lambda n_{21}^{(1)} + n_{11}^{(1)} &= 0.
\end{aligned} \tag{31}
$$

The first-order harmonic solution corresponding to the fundamental mode of the perturbation expansion can be obtained by retaining only the linear contributions in the lowest-order approximation. This solution describes the basic oscillatory behavior of the plasma species and forms the essential building block for the higher-order nonlinear analysis. In this approximation, all physical variables oscillate harmonically with respect to the fast-phase variable, while their amplitudes evolve slowly in space and time, thereby capturing the fundamental wave dynamics that govern the subsequent nonlinear evolution of the system. By applying the first-order harmonic analysis to the linearized perturbation Equation (31) and imposing the solvability condition for nontrivial solutions of the resulting algebraic system, we obtain the following linear dispersion relation governing the propagation of heavy ion-acoustic waves (HIAWs) in the considered magnetized plasma:

$$\omega^2 = \frac{-F \pm \sqrt{F^2 - 4GE}}{2G}. \tag{32}$$

where $F = -k^2\left(\omega_{c1}^2(1+\alpha^2) + 1 + \lambda\alpha\right) - T_1\omega_{c1}^2(1+\alpha^2)$, $E = \alpha\omega_{c1}^2\left(k^2(\alpha\omega_{c1}^2 + \alpha + \lambda) + \omega_{c1}^2\alpha T_1\right)$, $G = k^2 + T_1$. The requirement $F^2 > 4GE$ ensures that the dispersion relation admits real and physically meaningful values of the wave frequency ω. Under this condition, Equation (33) yields two distinct propagating modes determined by the choice of sign in ω. The positive root corresponds to the fast ion-acoustic mode (ω_f), whereas the negative root represents the slow ion-acoustic mode (ω_s). In the present analysis, we focus exclusively on the fast ion-acoustic mode, since in the considered plasma configuration, both light and heavy ion species oscillate coherently and remain in phase with the electron dynamics, thereby making the fast mode the dominant contributor to the nonlinear wave evolution.

In the limiting case of vanishing external magnetic field ($\omega_{c1} = 0$), Equation (33) reduces to $\omega^2 = \frac{k^2(1+\alpha\lambda)}{k^2+T_1}$, which is consistent with the dispersion relation previously reported by Chowdhury et al. [10]. The contributions corresponding to the second-order perturbation level $(m = 2)$ in conjunction with the first harmonics $(l = 1)$ yield to the following second-order equations [14]. These second-order equations together with the first harmonic $(l = 1)$ give the compatibility condition as

$$v_g = \frac{\dfrac{1}{\omega_{c_1}^2 - \omega^2} + \dfrac{\lambda\alpha}{\alpha^2\omega_{c_1}^2 - \omega^2} + 1}{-k\omega\left(\dfrac{\lambda\alpha}{(\alpha^2\omega_{c_1}^2 - \omega^2)^2} + \dfrac{1}{(\omega_{c_1}^2 - \omega^2)^2}\right)}. \tag{33}$$

Our analysis reveals that the amplitude of the second-order harmonics scales with the magnitude of $|\Psi_1^{(1)}|^2$ with coefficients C_i, where $i = 1, 2, 3, \ldots, 12$ generate from the analytical calculations of the plasma model and contain combinations of the associated plasma parameters. The complete analytical equations for these coefficients and detailed derivation of all coefficients C_i are provided in reference [14]. Finally, the evolution equations corresponding to the third harmonic ($m = 3$) and first-order perturbation ($l = 1$) are combined with Equations (18)–(22) to derive the standard NLSE describing the slow modulation of the carrier wave envelope, where $\Psi \equiv \Psi_1^{(1)}$:

$$i\frac{\partial \Psi(\xi,\tau)}{\partial \tau} + P\frac{\partial^2 \Psi(\xi,\tau)}{\partial \xi^2} + Q|\Psi(\xi,\tau)|^2\Psi(\xi,\tau) = 0. \tag{34}$$

where P and Q denote the group-dispersion and nonlinear coefficients, and are expressed as

$$\begin{aligned} P = -\frac{1}{2\omega k^2\left[\frac{\alpha\lambda}{(\alpha^2\omega_{c1}^2-\omega^2)^2}+\frac{1}{(\omega_{c1}^2-\omega^2)^2}\right]}\Bigg[&\frac{3k\alpha\omega\lambda v_g}{(\alpha^2\omega_{c1}^2-\omega^2)^2}+\frac{3k\omega v_g}{(\omega^2-\omega_{c1}^2)^2} \\ &+\left(\frac{k^2\alpha(3\omega^2+\alpha^2\omega_{c1}^2)\lambda}{(\alpha^2\omega_{c1}^2-\omega^2)^3}-\frac{k^2(3\omega^2+\omega_{c1}^2)}{(\omega^2-\omega_{c1}^2)^3}\right)v_g^2\Bigg]. \end{aligned} \tag{35}$$

$$\begin{aligned} Q = -\frac{1}{2\omega k^2\left(\frac{\alpha\lambda}{(\alpha^2\omega_{c1}^2-\omega^2)^2}+\frac{1}{(\omega_{c1}^2-\omega^2)^2}\right)}\Bigg[&-2T_2(C_7+C_{12})-3T_3+\frac{k^2(C_1+C_9)}{-\omega_{c1}^2+\omega^2} \\ &+\frac{2k^3\omega(C_2+C_8)}{(\omega_{c1}^2-\omega^2)^2}-\frac{\lambda k^2\alpha(C_4+C_{10})}{\alpha^2\omega_{c1}^2-\omega^2}+\frac{2\lambda\alpha k^3\omega(C_5+C_{11})}{(\alpha^2\omega_{c1}^2-\omega^2)^2} \\ &-2i\omega_{c1}k^3\left(\frac{\alpha^2C_6\lambda}{(\alpha^2\omega_{c1}^2-\omega^2)^2}-\frac{C_3}{(\omega_{c1}^2-\omega^2)^2}\right)\Bigg]. \end{aligned} \tag{36}$$

It is worth noting that both coefficients, P and Q, are real-valued functions of the carrier wave number k.

4. Dynamical System of Magnetized Heavy Ion-Acoustic Waves

In this section, we introduce a phase transformed wave amplitude and a traveling wave coordinate to study the nonlinear dynamical characteristics of the magnetized HIAWs according to $\chi = L\xi - \nu\tau$ and $\Psi(\chi) = \Phi(\chi)\exp(i\beta\chi)$ with $\Phi(\chi)$ being the real valued amplitude of the wave envelope, β representing the associated phase parameter, and v corresponding to the velocity of the wave propagation. Substituting these transformations into the NLSE (Equation (34)) yields the following ordinary differential equation:

$$PL^2\frac{d^2\Phi}{d\chi^2} + \left(\beta v\Phi - \beta^2PL^2\Phi + Q|\Phi|^2\Phi\right) + i\left(-v + 2PL^2\beta\right)\frac{d\Phi}{d\chi} = 0, \tag{37}$$

Here, $0 < L < 1$, while v represents the propagation speed of the traveling HIAWs. The corresponding amplitude equation from Equation (8) can be obtained from its real part in order to separate its real and imaginary components. Consequently, the spatial evolution of the wave amplitude is given as

$$\frac{d^2\Phi}{d\chi^2}\left(\beta^2 - \frac{\beta v}{PL^2}\right)\Phi - \frac{Q}{PL^2}\Phi^3. \tag{38}$$

This equation signifies a second-order nonlinear dynamical equation describing the dynamics of the traveling wave amplitude. It provides the basic framework for exploring the associated dynamical behaviors and nonlinear structures of the magnetize HIAWs in the present theoretical framework. However, Equation (38) can be transformed into an equivalent first-order dynamical system in the phase-space variables (Φ, z) as

$$\begin{cases} \dfrac{d\Phi}{d\chi} = z, \\ \dfrac{dz}{d\chi} = M_1\Phi - M_2\Phi^3, \end{cases} \tag{39}$$

Here, the parameters M_1 and M_2 are defined by $M_1 = \beta^2 - \frac{\beta v}{PL^2}$ and $M_2 = \frac{Q}{PL^2}$. The corresponding Hamiltonian, which remains invariant through the trajectories of the dynamical system can be written as

$$H(\Phi, z) = \frac{z^2}{2} - \frac{M_1\Phi^2}{2} + \frac{M_2\Phi^4}{4} = h. \tag{40}$$

where h represents the constant Hamiltonian related with a precise phase-space orbit. By reorganizing this energy integral, the first-order traveling wave equation can be obtained in factored form as

$$\frac{d\Phi}{d\chi} = \sqrt{-\frac{M_2}{2}(p_1 - \Phi)(\Phi - p_2)(\Phi - p_3)(\Phi - p_4)}. \tag{41}$$

where p_1, p_2, p_3, and p_4 denote the roots of the Hamiltonian equation $h_i - \frac{M_2}{2}\left(\Phi^4 - \frac{2M_1}{M_2}\Phi^2\right) = 0$. Here, the subscript i denotes an arbitrary initial point in the phase-space plane, characterized by the coordinates (Φ_i, z_i), and $h_i = H(\Phi_i, z_i)$ represents the corresponding constant Hamiltonian energy level. Therefore, the above equation describes the traveling-wave trajectories of the magnetized plasma system passing through the selected phase-space point (Φ_i, z_i). To further investigate the dynamical behavior of the system, we consider the vector field associated with Equation (10), defined as $\mathbf{F} = \left(z, , M_1\Phi - M_2\Phi^3\right)$. Thus,

$$\nabla \cdot \mathbf{F} = \frac{\partial}{\partial\Phi}(z) + \frac{\partial}{\partial z}\left(M_1\Phi - M_2\Phi^3\right) = 0. \tag{42}$$

The conservative nature of this dynamical system is demonstrated by $\nabla \cdot \mathbf{F} = 0$, which indicates that every trajectory evolves a constant Hamiltonian energy level. The unperturbed HIAW state is represented by the saddle point $N_0 = (0, 0)$ and the system also has two nonzero equilibria N_1 and N_2 that are symmetrically placed on both the positive and negative potential lobes. The positions of these symmetric centers are given by $\Phi_c = \pm\sqrt{M_1/M_2}$, and they arise from the cubic nonlinear contribution $-M_2\Phi^3$ and the linear term $M_1\Phi$. The important homoclinic separatrix that joins the saddle point N_0 in the asymptotic limit is represented by the NHT_2 trajectory. The amplitude between the inner and outer nonlinear dynamical regimes is established by $\Phi_s = \pm\sqrt{2M_1/M_2}$, which also determines the maximal homoclinic amplitude. A supernonlinear periodic state with a Hamiltonian energy above the homoclinic separatrix is represented by outer SPT_3 trajectory. The Hamiltonian is invariant under the polarity-reversal transformation $\Phi \to -\Phi$, such that $H(-\Phi, z) = H(\Phi, z)$. Consequently, the phase-space trajectories exhibit reverse profile about the z-axis, indicating that the positive- and negative-polarity wave structures possess identical dynamical characteristics (for example, see Figure 1).

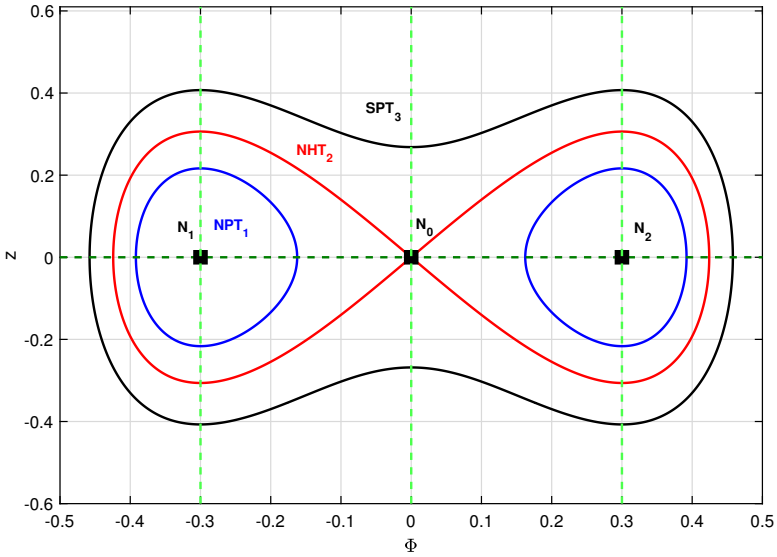


Figure 1. Representative phase-space trajectories of the nonlinear periodic trajectory NPT_1 (blue), nonlinear homoclinic trajectory NHT_2 (red), and superperiodic trajectory SPT_3 (black) for $\beta = 0.2$, $v = 0.3$, $L = 0.2$, $k = 0.6$, $\alpha = 0.5$, $\sigma = 0.5$, $\omega_{c1} = 0.5$, $\mu_e = 0.5$, $\mu_p = 0.3$, $q = 0.6$, $\kappa = 3$, and $\alpha_e = 0.3$.

The potential impact of the magnetic field through ω_{c1}(=0.3, 0.5, 0.7, and 0.9) on the nonlinear phase-space dynamics of magnetized HIAWs) is examined, as shown in Figure 2. The trajectories gradually extend in the z-direction as ω_{c1} increases, signifying an increased phase-space velocity $z = d\Phi/d\chi$. The equilibrium points along the Φ-axis are nearly unaffected, while the nonlinear periodic trajectories NPT_1 expand around their centers. Stronger vertical expansion in the homoclinic trajectories NHT_2 is shown, where the maximum $|z|$ increases steadily with $\omega c1$, suggesting higher spatial gradients of magnetized HIAWs. The supernonlinear periodic trajectories SPT_3 show that the strongest magnetic field responses attain their largest phase-space excursion at $\omega c1 = 0.9$. At the Hamiltonian level, their progressive outward expansion suggests gradually stronger nonlinear excursions. However, even under the strong magnetic field, the trajectories NPT_1, NHT_2, and SPT_3 maintain their characteristics topology, while the field controls the magnitude and strength of nonlinear dynamics without inducing topological transitions. In conclusion, without changing the nonlinear trajectory classification of periodic, homoclinic, and supernonlinear magnetized HIAW states, an increase in the normalized cyclotron frequency systematically increases the phase-space excursion and gradient strength.

Three amplitude-controlled nonlinear regimes for $\Phi_{NPT} = \pm 0.90\Phi_S$, $\Phi_{NHT} = \pm\Phi_S$, and $\Phi_{SPT} = \pm 1.10\Phi_S$ are revealed by the spatial evolution of magnetized HIAWs, with red and black curves representing negative and positive initial branches, respectively (see Figure 3). These magnetized HIAW profiles are analyzed with fixed parameters $\beta = 0.2$, $v = 0.3$, $l = 0.2$, $k = 0.6$, $\alpha = \sigma = 0.5$, $\omega_{c1} = \mu_p = 0.3$, $\mu_e = 0.5$, $\kappa = 3$, and $\alpha_e = 0.3$. The finite amplitude oscillations arise at nonzero equilibria for Ψ_{NPT}, as shown in Figure 3a. Each branch exhibits closed-orbit periodicity without polarity reversal by staying inside its initial potential domain. Sharply localized pulses with tails that are close to equilibrium appear at the separatrix $\Phi_{NHT} = \pm\Phi_S$ (e.g., see Figure 3b). The displacement between opposite polarity pulses indicates different original phases rather than polarity switching, and such patterns are the real space homoclinic trajectories. The SPT states exhibit large-amplitude oscillations beyond the separatrix and explore both compressive and rarefactive potential domains and repeatedly crossing $\Phi = 0$, as shown in Figure 3c. These profiles show how highly sensitive HIAW morphology is to the initial energy level with fixed

$\beta = 0.2$, $v = 0.3$, $l = 0.2$, $k = 0.6$, $\alpha = \sigma = 0.5$, $\omega_{c1} = \mu_p = 0.3$, $\mu_e = 0.5$, $\kappa = 3$, and $\alpha_e = 0.3$.

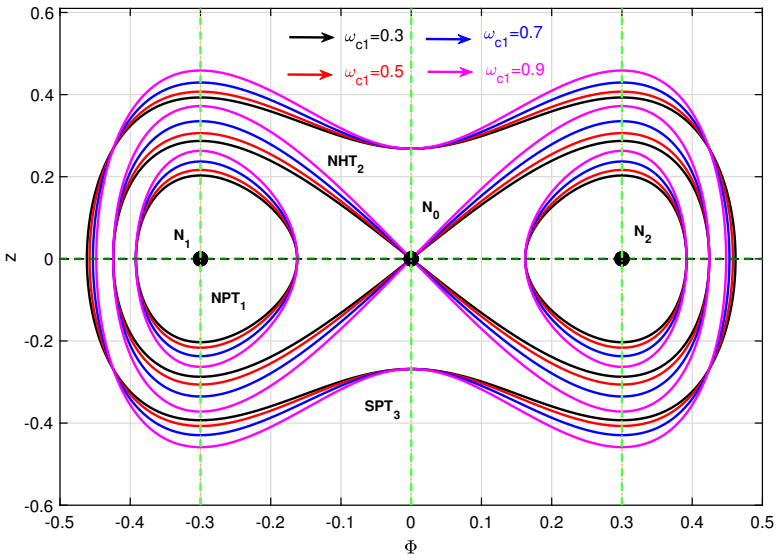


Figure 2. Phase-space evolution of the nonlinear periodic trajectory NPT_1, nonlinear homoclinic trajectory NHT_2, and superperiodic trajectory SPT_3 wave states for $\omega_{c1} = 0.3$ (black), 0.5 (red), 0.7 (blue), and 0.9 (magenta). The remaining fixed parameters are $\beta = 0.2$, $v = 0.3$, $L = 0.2$, $k = 0.6$, $\alpha = 0.5$, $\sigma = 0.5$, $\mu_e = 0.5$, $\mu_p = 0.3$, $q = 0.6$, $\kappa = 3$, and $\alpha_e = 0.3$.

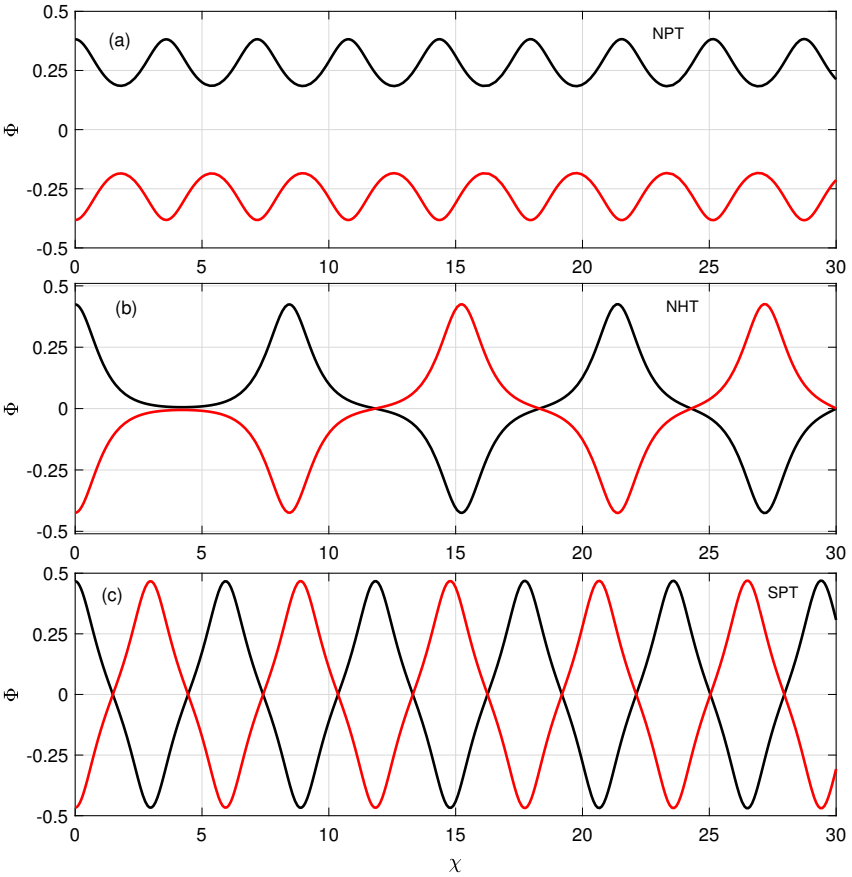


Figure 3. Hamiltonian reversal polarity symmetry of the (**a**) NPT, (**b**) NHT, and (**c**) SPT wave profiles for $\Phi_{NPT} = 0.90\Phi_S$, $\Phi_{NHT} = \Phi_S$, and $\Phi_{SPT} = 1.10\Phi_S$. The positive and negative polarities are represented by the colors black and red, respectively. The fixed parameters are $\beta = 0.2$, $v = 0.3$, $L = 0.2$, $k = 0.6$, $\alpha = 0.5$, $\sigma = 0.5$, $\omega_{c1} = 0.3$, $\mu_e = 0.5$, $\mu_p = 0.3$, $\kappa = 3$, and $\alpha_e = 0.3$.

We examine the effect of the magnetic gyromotion through ω_{c1} on NPT, NHT, and SPT for $\Phi_{\rm NPT} = 0.90\Phi_S$, $\Phi_{\rm NHT} = \Phi_S$, and $\Phi_{\rm SPT} = 1.10\Phi_S$, which governs the nonlinear spatial scales of HIAWs (e.g., see Figure 4). Here, the black curve is for $\omega_{c1} = 0.3$ and the red curve is for $\omega_{c1} = 0.7$. With a strong magnetic field, the characteristic phase-space regime remains unchanged under fixed plasma parameters defined for Figure 3. In Figure 3a, the nonlinear periodic HIAW continues to be a bounded positive potential oscillatory for both magnetic-field strengths, while its spatial recurrence is prominently modified by increasing ω_{c1}. In Figure 4b, the NHT counterpart solution exhibits a considerably stronger variation with magnetic field ω_{c1}, as the positive and negative peaks are shifted leftward of the potential. Therefore, the homoclinic energy is moved by magnetic gyromotion without losing its separatrix-controlled localization. Large amplitude polarity-crossing oscillations are still present in the SPT condition in Figure 4c, and a higher spatial oscillation rate is indicated by its shorter wavelength. The normalized cyclotron frequency modifies the phase accumulation and nonlinear wavelength, while the characteristic morphologies of the NPT, NHT, and SPT structures remain unchanged.

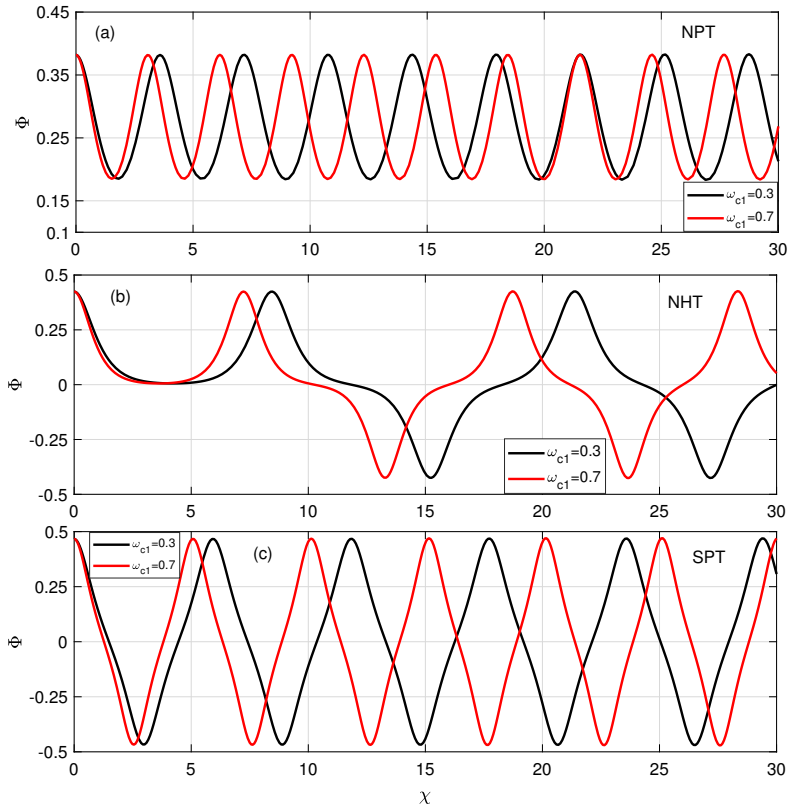


Figure 4. Variations in (**a**) NPT, (**b**) NHT, and (**c**) SPT waves under magnetic-field strengths for $\omega_{c1} = 0.3$ (black) and 0.7 (red), with $\Phi_{\rm NPT} = 0.90\Phi_S$, $\Phi_{\rm NHT} = \Phi_S$, and $\Phi_{\rm SPT} = 1.10\Phi_S$. The fixed plasma parameters are $\beta = 0.2$, $v = 0.3$, $\ell = 0.2$, $k = 0.6$, $\alpha = 0.5$, $\sigma = 0.5$, $\mu_e = 0.5$, $\mu_p = 0.3$, $\kappa = 3$, and $\alpha_e = 0.3$.

The spatial dynamics of magnetized HIAWs are also governed by the traveling wave velocity v, as depicted in Figure 5, where $v = 0.2$ and $v = 0.5$ are represented by black and red curves, respectively. The separatrix threshold Φ_S is used to prescribe the positive initial branches: $\Phi_{\rm NPT} = 0.90\Phi_S$ (subseparatrix), $\Phi_{\rm NHT} = \Phi_S$ (separatrix), and $\Phi_{\rm SPT} = 1.10\Phi_S$ (superseparatrix). Both NPT states in Figure 5a are constrained in the regime $\Phi > 0$. The recurrence length between two successive peaks with wave velocity is shortened and causes a cumulative phase shift. Figure 5b shows a more robust response: for $v = 0.5$, the NHT extrema shift spatially and become closer together, while their near-zero tails

maintain homoclinic localization. Large-amplitude polarity crossing oscillations are still present in the NHT in Figure 5c. The source of this behavior is $\Delta_1 = \beta^2 - \beta v/(Pl^2)$, where v alters the effective nonlinear length scale. This velocity-induced compression, which packs coherent HIAW energy onto shorter spatial scales without inclusive structural destabilization, physically reflects a changed equilibrium among magnetic confinement, dispersion, and nonlinearity. Unlike magnetic-field variation, which modifies the nonlinear spatial dynamics through ion gyromotion, the traveling-wave velocity influences the effective nonlinear length scale through Δ_1, thereby controlling pulse spacing and spatial recurrence while preserving the underlying phase-space topology.

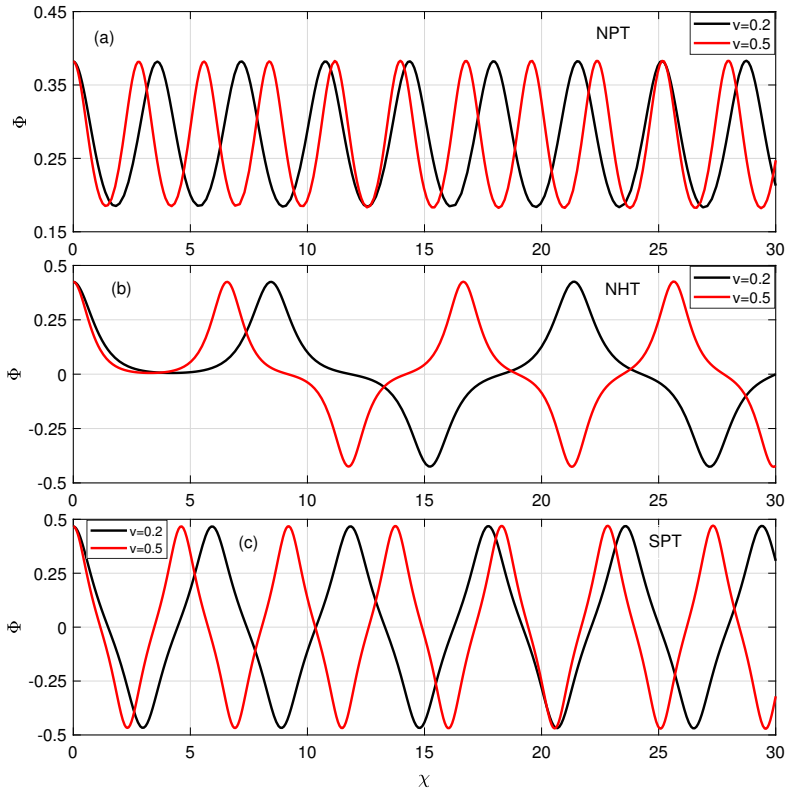


Figure 5. Evolution of (**a**) NPT, (**b**) NHT, and (**c**) SPT waves under propagation velocity for $v = 0.2$ (black) and 0.5 (red), with $\Phi_{\mathrm{NPT}} = 0.90\Phi_S$, $\Phi_{\mathrm{NHT}} = \Phi_S$, and $\Phi_{\mathrm{SPT}} = 1.10\Phi_S$. The fixed plasma parameters are $\beta = 0.2$, $L = 0.2$, $k = 0.6$, $\alpha = 0.5$, $\omega_{c1} = 0.3$, $\sigma = 0.5$, $\mu_e = 0.5$, $\mu_p = 0.3$, $\kappa = 3$, and $\alpha_e = 0.3$.

The phase portrait possesses three equilibrium points N_i at $(\Phi_i, 0)$, where $i = 0, 1, 2$. The Hamiltonian criterion $H(\Phi, z) = 0$ is evaluated at N_0 which generates the nonlinear homoclinic orbits that correspond to localized solitary wave structures. Employing the basic algebraic procedures, the final first-order differential equation is separated and integrated under the localized boundary conditions $\Phi \to 0$ as $|\chi| \to \infty$ using $z = d\Phi/d\chi$ in the Hamiltonian equation. Here, the localized sech-type solitary wave solution is derived as

$$\Phi(\chi) = \pm\sqrt{\frac{2M_1}{M_2}}\,\mathrm{sech}\left(\sqrt{M_1}\chi\right). \tag{43}$$

The dual-polarity plasma system's compressive and rarefactive solitary structures are represented by the positive and negative branches of this solution, respectively.

The solitary wave profiles show the non-Maxwellian kinetics and magnetic confinement control rarefactive ($\Phi < 0$, dashed) and compressive ($\Phi > 0$, solid) magnetized HIAWs, as shown in Figure 6. In Figure 6a, the peak amplitudes of both rarefactive and compressive solitary waves are progressively reduced with stronger magnetic-field strength

through ω_{c1}. The magnetic field controls the electrostatic response and dramatically modifies the dispersion and nonlinearity balance. Raising superthermal electrons κ from 3 to 5 in Figure 6b decreases the amplitudes because the plasma is driven toward Maxwellian behavior by weaker superthermal electron tails. On the other hand, ion nonextensivity controls the nonlinear restoring force without changing localization behavior, as shown in Figure 6c, which shows that increasing q from 0.3 to 0.9 weakens both rarefactive and compressive branches. When the carrier wavenumber k increases from 0.6 to 0.8, Figure 6d shows the highest suppression; the shorter carrier scale increases dispersive competition and constrains the possible excursion. Equal positive and negative magnitudes maintain polarity reversal symmetry. Their similar widths further suggest that these parameters do not cause a polarity selective bifurcation and coherent solitary wave organization in the magnetized plasma, but rather primarily redistribute nonlinear electrostatic energy. In conclusion, these plasma parameters in Figure 6 systematically shrink the magnitude of compressive and rarefactive magnetized HIAW solitary waves while maintaining their symmetric bipolar localized structure.

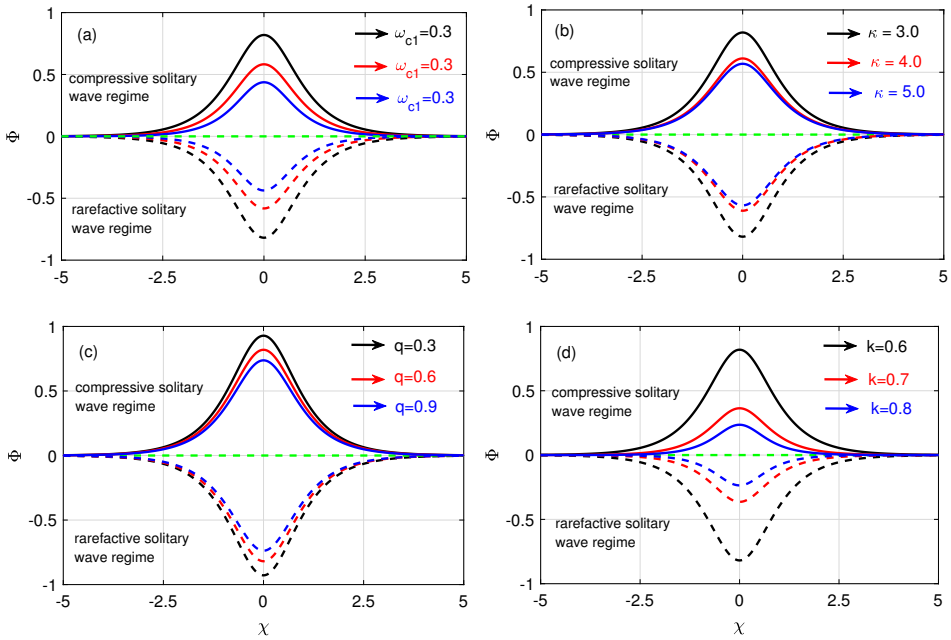


Figure 6. Parametric modulation of the compressive (solid) and rarefactive (dashed) solitary-wave profiles for (**a**) $\omega_{c1} = 0.3, 0.5, 0.7$, (**b**) $\kappa = 3, 4, 5$, (**c**) $q = 0.3, 0.6, 0.9$, and (**d**) $k = 0.6, 0.7, 0.8$ (black, red, and blue, respectively). The remaining parameters are $\beta = 0.2$, $v = 0.3$, $\ell = 0.2$, $\alpha = 0.5$, $\sigma = 0.5$, $\mu_e = 0.5$, $\mu_p = 0.3$, and $\alpha_e = 0.3$.

5. Modulational Instability and Growth-Rate Analysis

5.1. Modulational Instability Criterion and Stability Regions

The change in (P/Q) with the carrier wavenumber (k) for various field strengths $\omega_{c1} = 0.4, 0.5, 0.6)$ at a fixed charged-weighted ion mass ratio $(\alpha = 0.5)$ is shown in Figure 7a. In this figure, enhancing the magnetic-field strength ω_{c1} shifts the first MI onset toward larger k. The presence of two disconnected instability regions (R_2) is separated by a wide stable domain (R_1).The instability thresholds move toward larger k-limit while they decrease towards smaller carrier wavenumbers when the field strength enhances. The MI onset changes conversely when ω_{c1} rises from 0.4 to 0.6 at low and high wavenumbers. As a result, the width of the stable region (R_1) becomes modified, indicating that the magnetic field has a significant impact on the balance between wave dispersion and nonlinear self-focusing. All curves in the middle wavenumber region show the stability threshold of

$(P/Q \approx 0)$ around the blue rectangle, where the weak nonlinear modulation balanced the dispersion. The impact of the electron concentration (μ_e) is seen in Figure 7b. Here, we observe the same stability profiles: the dual stability-instability regions shift conversely with electron concentration (μ_e). This behavior suggests that the weak electron concentration (μ_e) typically broadens the range of stable HIAW propagation by shifting the MI onset in the left stable region R_1. Physically, a stronger magnetic field modifies the dispersive properties of the magnetized HIAWs and increases ion gyromotion, which in turn modifies the onset conditions for MI.

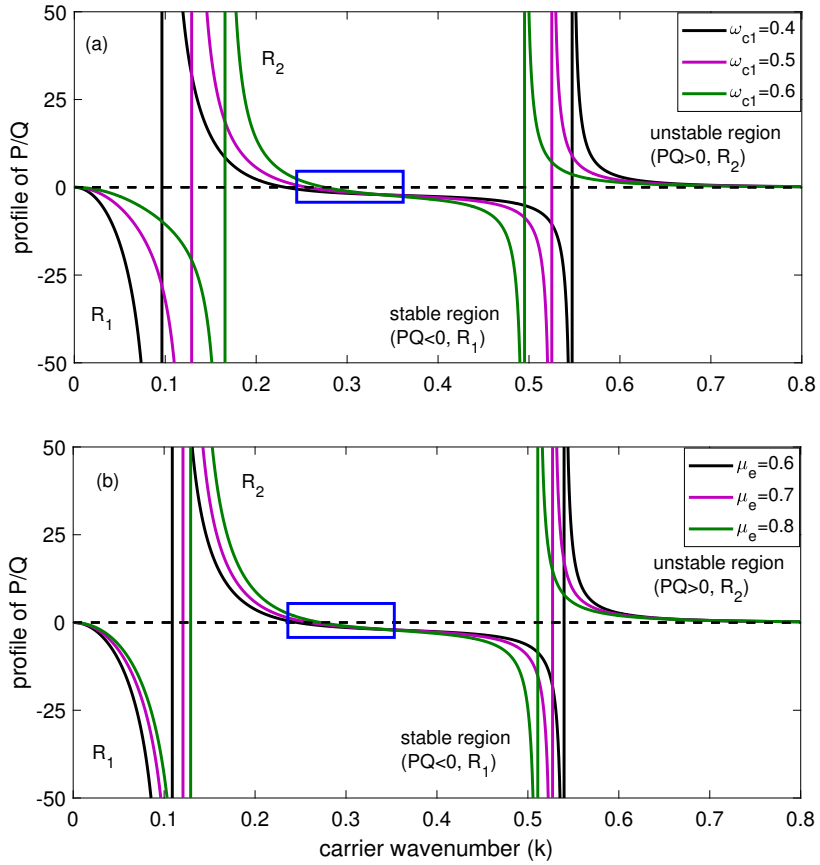


Figure 7. Profiles of P/Q versus the carrier wavenumber k for magnetized HIAWs: (**a**) $\omega_{c1} = 0.4$, 0.5, and 0.6 at $\mu_e = 0.5$, and (**b**) $\mu_e = 0.6$, 0.7, and 0.8 at $\omega_{c1} = 0.4$. The $P/Q < 0$ regions denote modulationally stable domains supporting dark envelope solitons, whereas $P/Q > 0$ identifies unstable domains favorable for bright envelope solitons. The fixed parameters are $\kappa = 3.0$, $\mu_p = 0.3$, $q = 0.6$, $\sigma = 0.5$, $\alpha = 0.5$, and $\alpha_e = 0.3$.

The MI spectrum of magnetized HIAWs under the spectral index (κ) (κ-Cairns distribution) and nonextensive parameter q (nonextensive distribution function) against the carrier wavenumber is shown in Figure 8a. Figure 8a illustrates the influence of index κ(=2.8, 3.0, 4.0) for fixed $q = 0.6$. For all values of κ, the wave packets remain modulationally stable $(P/Q < 0)$ at weak carrier wavenumbers. The P/Q changes sign at the critical wavenumber k_c, indicating the transition to MI. The strongest superthermal case, $\kappa = 2.8$, exhibits the largest positive peak, implying that nonlinear self-focusing dominates dispersion and strongly favors the formation of localized envelope structures. The peaks of the P/Q reduce significantly with κ and P/Q profiles become smoother. The magnetized HIAWs become marginally unstable at larger k-limit. The inset figure further examines the nearly Maxwellian regime $(\kappa = 5.0, 7.0, 10.0)$, where both the stable and unstable branches vary marginally. This demonstrates that increasing κ suppresses MI by weakening the

influence of energetic superthermal electrons and enhancing stable wave propagation. Figure 8b shows the effect of the nonextensive parameter q at the fixed spectral index $\kappa = 3.0$. All curves exhibit the same stability topology, with P/Q changing from negative to positive at large k-limits. Both the negative minimum and the positive maximum of P/Q vary monotonically, producing a smoother transition from stable to unstable regions. The electron superthermality and the nonextensive parameter control the onset and strength of MI, while P/Q vary non-monotonically and monotonically, respectively. The P/Q profiles have a similar trend to the earlier findings by Douanla et al. [14].

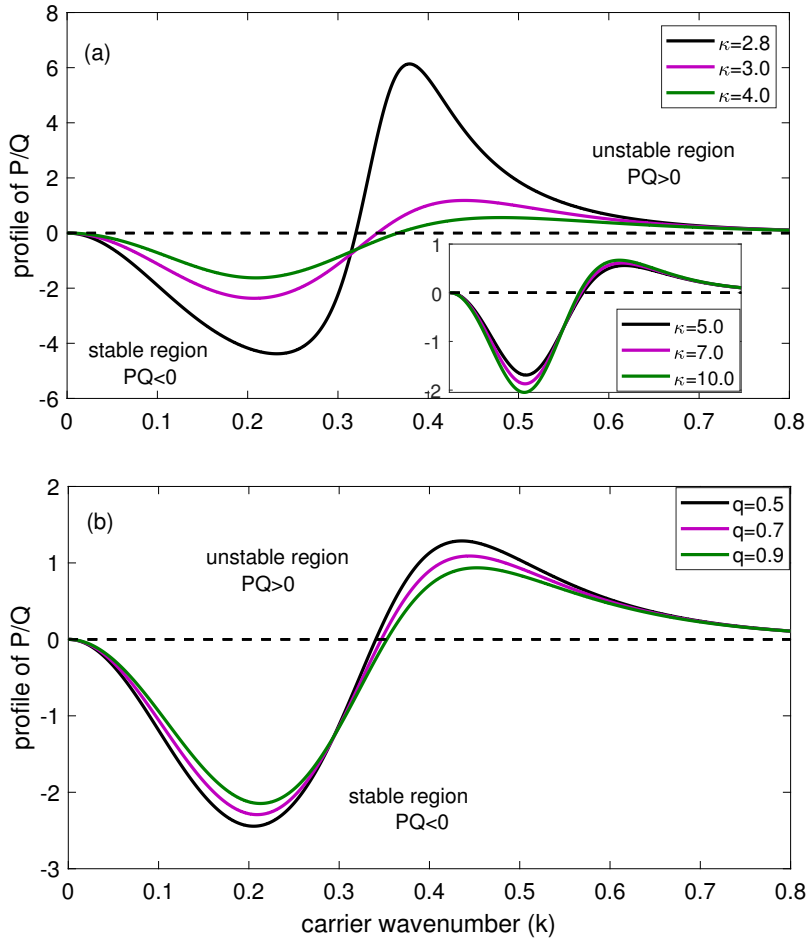


Figure 8. Profiles of P/Q as a function of k for magnetized HIAWs: (**a**) $\kappa = 2.8$, 3.0, and 4.0 at $q = 0.6$, with the inset showing $\kappa = 5.0$, 7.0, and 10.0, and (**b**) $q = 0.5$, 0.7, and 0.9 at $\kappa = 3.0$. The remaining plasma parameters are $\alpha = 0.5$, $\sigma = 0.5$, $\omega_{c1} = 0.8$, $\mu_e = 0.8$, $\mu_p = 0.3$, and $\alpha_e = 0.3$.

The potential impact of the positron concentration (μ_p) for a fixed temperature ratio $\sigma = 0.5$ on P/Q is shown in Figure 9a. All three curves exhibit the same multi-branch topology, which consists of two stable regions (R_1) separated by an intermediate unstable branch (R_2). The low-k stable (dark-soliton) region moves toward higher carrier wavenumbers with high positron concentration (from 0.6 to 0.8), whereas the high-k stable region shifts toward lower carrier wavenumbers. The central stable branch also shrinks, indicating that a higher positron concentration promotes the onset of MI. Consequently, the parameter space supporting bright envelope solitons and rogue-wave excitation expands as the positron population increases. Figure 9b shows the influence of the ratio of ion-to-electron temperature through the nonextensive distribution σ at the fixed positron concentration $\mu_p = 0.8$. Increasing σ from 0.3 to 0.9 noticeably shifts the first and second singularities in different carrier wavenumber regimes. The rectangular region demonstrates that the P/Q

profiles approach the stability threshold as σ increases, suggesting that the competition between dispersion and nonlinearity becomes strongly sensitive to small variations in the temperature ratio. A comparison of both Figure 9a,b reveal that the positron concentration and the temperature ratio similarly control the stability topology by shifting the critical wavenumbers and separate stable and unstable domains. However, the temperature ratio produces a more pronounced shift in the stability boundaries, demonstrating that thermal effects play a dominant role in stability analysis.

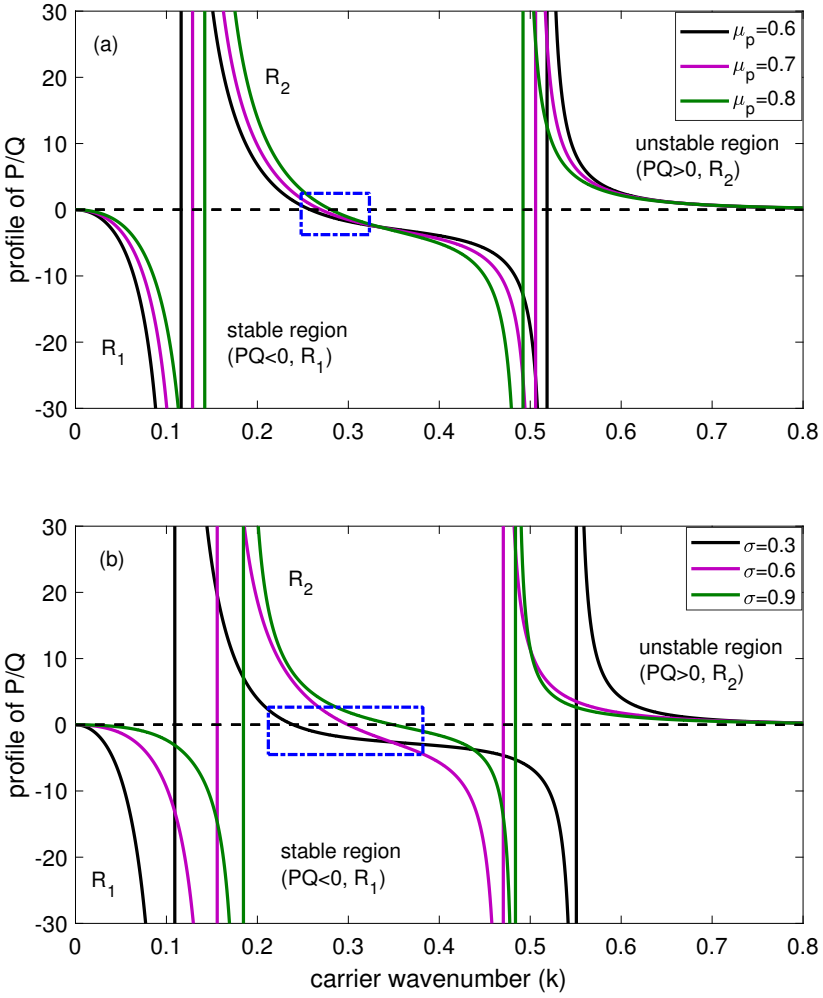


Figure 9. Profiles of P/Q versus the carrier wavenumber k for magnetized HIAWs: (**a**) $\mu_p = 0.6$, 0.7, and 0.8 at $\sigma = 0.5$, and (**b**) $\sigma = 0.3$, 0.6, and 0.9 at $\mu_p = 0.8$. The regions with $P/Q < 0$ denote modulationally stable domains, whereas $P/Q > 0$ represents modulationally unstable domains. The remaining plasma parameters are $\alpha = 0.5$, $\omega_{c1} = 0.4$, $\mu_e = 0.4$, $\kappa = 3.0$, and $\alpha_e = 0.3$.

5.2. Contour Maps of Modulational Stability

The contour plots reveal the P/Q sign and its magnitude, which are strongly impacted by carrier wavenumber k, charge-weighted ion mass ratio α, and the superthermality κ. The solid black transition curves show the critical conditions where the P/Q changes polarity. The ratio P/Q determines the modulational dynamics of magnetized HIAW packets with domains of $P/Q < 0$ supporting the dark envelope solitons and the regions with $P/Q > 0$ may develop bright envelope solitons, breathers, and rogue-wave excitations. Figure 10a shows two separate stable domains for spectral index $\kappa = 3.0$, separated by their respective unstable regions. The α-value has a significant impact on the left unstable region $R_2(0.06 < k < 0.23)$, which appears in a narrow band at smaller carrier wavenumber

limit. This suggests that the coupling between light positive ions and heavy negative ions can destabilize the bright soliton when the charge-weighted ion mass ratio changes even at relatively small k. A broad stable region $R_1(0.23 < k < 0.66)$ appears, where $P/Q < 0$ between the two instability boundaries demonstrates that dispersion controls the nonlinear self-focusing effect and constrains the expansion of envelope perturbations. The system again enters an unstable regime at larger k-limit where $P/Q > 0$, suggesting that short-wavelength magnetized HIAW packets become advantageous for the development of localized bright envelope structures. Figure 10b signifies the corresponding stability profile for a larger spectral index, where the particle distribution approaches the Maxwellian limit. The qualitative topology remains unchanged and the stability boundaries shift noticeably. The left stable region (R_1) changes marginally in the (k, α)-plane with index κ, while the intermediate stable region (R_1) shrinks. A comparison of Figure 10a,b clearly demonstrates that the spectral index (κ) acts as an effective control parameter governing the stability topology of magnetized HIAWs. As a result, the stability boundaries are significantly modified, which indicate a stronger dependence of the MI threshold on both k and α. These two-dimensional cuts exactly match the transitions depicted in the 1D P/Q plots, which indicate a wide stable domain (R_1) surrounded by two discontinuous unstable zones (R_2).

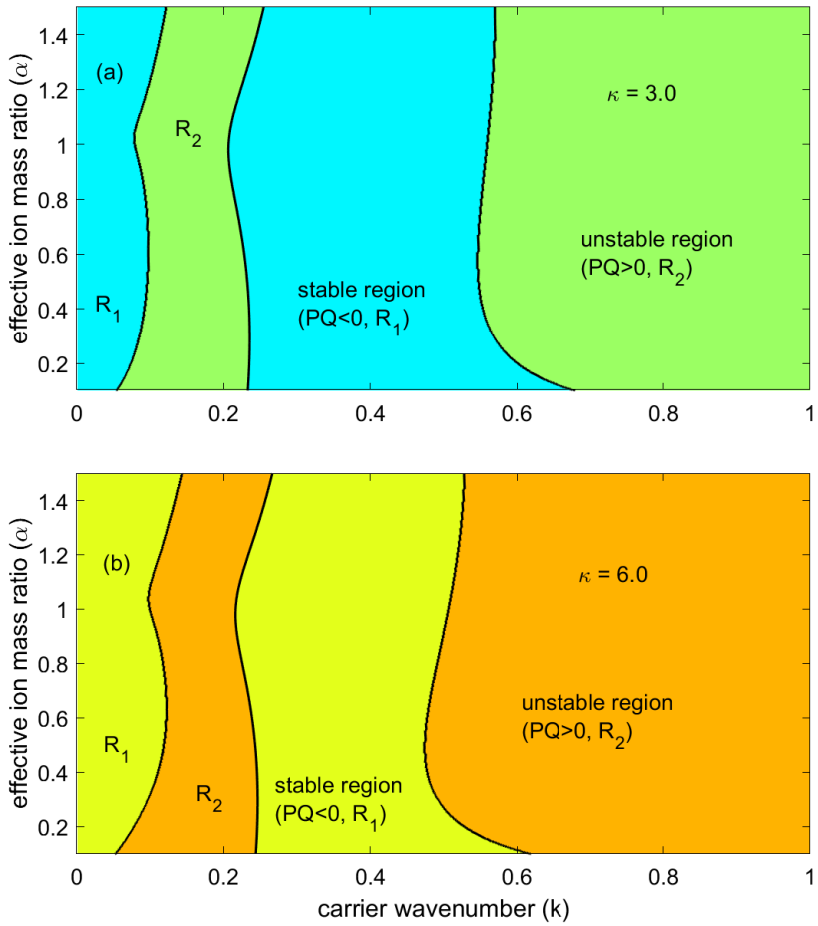


Figure 10. Contour plots of the ratio P/Q in the (k, α)-plane for magnetized HIAW plasmas with (**a**) $\kappa = 3.0$ and (**b**) $\kappa = 6.0$. The regions with $PQ < 0$ (R_1) represent modulationally stable domains supporting dark envelope solitons, whereas the regions with $PQ > 0$ (R_2) correspond to modulationally unstable domains. The fixed parameters are $\omega_{c1} = 0.4$, $\mu_e = 0.5$, $\mu_p = 0.3$, $q = 6.0$, $\sigma = 0.5$, and $\alpha_e = 0.3$.

For two distinct magnetic-field strengths, (a) $\omega_{c1} = 0.65$ and (b) $\omega_{c1} = 0.75$, the contour plots show the MI spectrum against the wavenumber (k) and the charge-weighted ion mass ratio (α). For moderate magnetic-field strength $\omega_{c1} = 0.65$ shown in Figure 11a, the

stability topology consists of two disconnected modulationally stable regions (denoted by R_1), separated by a broad unstable domain (denoted by R_2) at larger carrier wavenumbers. The charged-weighted ion mass ratio α between light positive and heavy negative ions substantially controls the MI onset at low k-limit, as evidenced by the left region R_1. Beyond a critical carrier wavenumber $(k \simeq 0.5)$, the system enters the $PQ > 0$ regime, indicating that nonlinear self-focusing dominates over dispersion and promotes the growth of MI. For the strong magnetic-field strength $(\omega_{c1} = 0.75)$ [Figure 11b], the overall stability topology is significantly modified. The left stability region $R_1(0 < k < 0.16)$ broadens and squeezes the right stability region in the intermediate k-limit $(0.28 < k < 0.68)$, indicating that a stronger magnetic field suppresses the onset of MI over a broader interval of propagation. The findings show that both the magnetic-field strength (ω_{c1}) and the charge-weighted ion mass ratio (α) also serve as effective control parameters for modulational stability in magnetized HIAWs. With increasing effective ion mass ratio α, the stability boundaries initially exhibit nonlinear variations, whereas at higher values of α, they approach nearly vertical profiles. This behavior suggests that the transition wavenumbers become weakly dependent on α, indicating an approximately saturated stability configuration within the investigated parameter range.

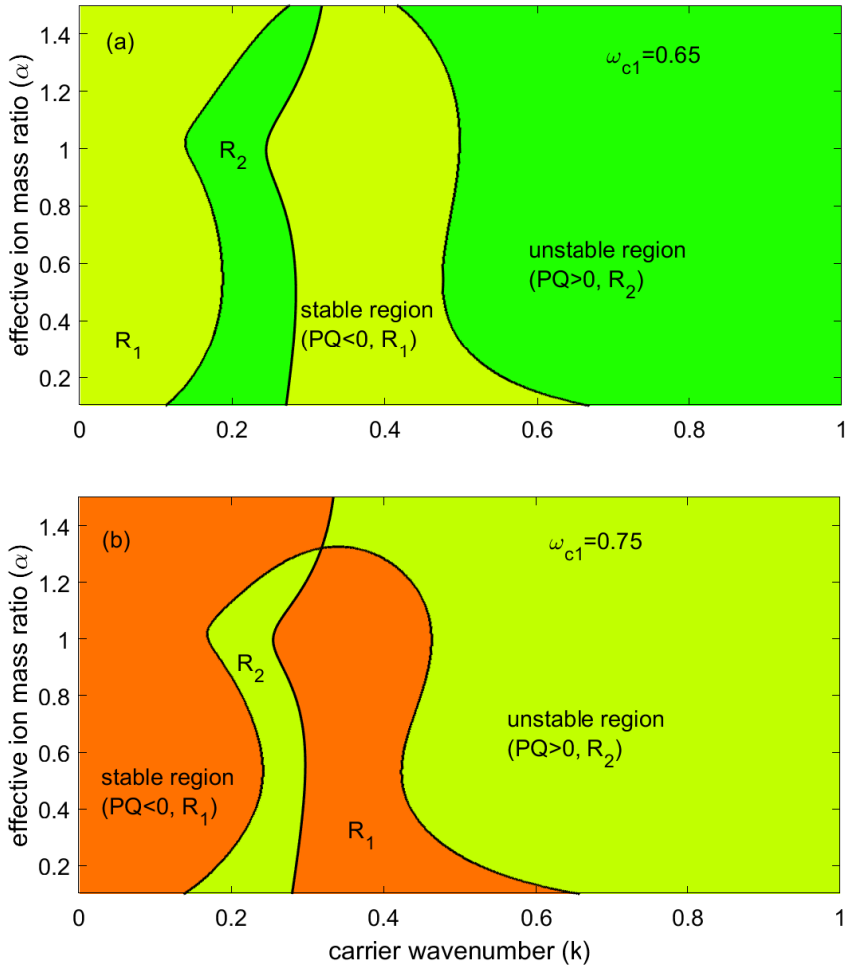


Figure 11. Contour plots of the ratio P/Q in the (k, α)-plane for magnetized HIAW plasmas with (**a**) $\omega_{c1} = 0.65$ and (**b**) $\omega_{c1} = 0.75$. The regions R_1 $(PQ < 0)$ denote modulationally stable domains supporting dark envelope solitons, whereas the $PQ > 0$ (R_2) regions represent modulationally unstable domains where bright envelope solitons can form. The remaining plasma parameters are $\kappa = 3.0$, $\mu_e = 0.5$, $\mu_p = 0.3$, $q = 6.0$, $\sigma = 0.5$, and $\alpha_e = 0.3$.

5.3. Modulational Instability Growth Rate

The envelope dynamics described by Equation (37) are governed entirely by the interplay between the dispersion coefficient P and the nonlinear coefficient Q. Since both coefficients depend on the plasma parameters α, σ, μ_e, μ_p, q, and ω_{c1}, variations in these parameters directly influence the MI of the magnetized HIAWs. The stability criterion is determined by the sign of the product PQ: the condition $PQ < 0$ corresponds to a modulationally stable region supporting dark envelope structures, whereas $PQ > 0$ identifies a modulationally unstable region where the carrier wave is susceptible to perturbations, giving rise to bright envelope solitons [18,58]. The boundary separating these two regimes is defined by the critical wave number k_c, at which the P/Q curve intersects the k-axis. Accordingly, the growth rate of MI is given by [18]

$$|\mathrm{Im}(\Omega)| = |PK|\sqrt{2\frac{Q}{P}\Psi_0^2 - K^2}. \tag{44}$$

where K denotes the modulation wavenumber. Equation (40) predicts a positive growth rate only for perturbation wave numbers satisfying $K < k_c = \sqrt{2Q/|P|}\,\Psi_0$, which requires the coefficients product to be positive ($PQ > 0$). Here, Ψ_0 represents the constant amplitude of the wave packets.

5.4. Dependence of MI Growth Rate on Plasma Parameters

The MI growth rate $(\mathrm{Im}(\Omega))$ of magnetized HIAWs is plotted versus the modulation wavenumber (K), emphasizing the significance of the magnetic field (ω_{c1}) at two carrier wavenumbers regimes, $k = 0.2$ and $k = 0.6$, respectively. Figure 12a corresponds to the smaller carrier wavenumber $(k = 0.2)$ connected to the left unstable domain R_2. The peak MI growth rate and unstable modulation bandwidth substantially reduce with magnetic field through ω_{c1} toward smaller values of K-limit. The maximum MI growth rate increases from approximately 0.7×10^{-3} to 2.9×10^{-3}, accompanied by a noticeable decrease in the cutoff modulation wavenumber. Figure 12b presents the corresponding MI spectra for the larger carrier wavenumber $(k = 0.6)$ associated with the right unstable region (R_2). The opposite trend is observed, although the instability becomes significantly stronger than in Figure 12a. For every value of ω_{c1}, both the peak growth rate and the unstable modulation bandwidth are considerably larger than those at $k = 0.2$, demonstrating that carrier waves with larger wavenumbers are inherently more susceptible to MI. The magnetic field's dual function of destabilizing in substantially nonlinear regimes and stabilizing in weakly dispersive regimes results from its conflicting effects on wave dispersion and ion gyromotion. We examine the MI growth rate under different plasma parameters, elucidating the impact of superthermality (κ) and the nonextensive parameter (q) (i.e., see Figure 12c,d). The profile of the MI growth rate begins at zero at $K = 0$, reaches a maximum, and disappears at a large modulation wavenumber. The potential impact of the nonextensive parameter $q(= 0.5, 0.7, 0.9)$ is shown in Figure 12d. As the parameter q rises, a monotonic enhancement at large modulation K-regime of MI is observed. Stronger nonextensivity intensifies the nonlinear coupling, as shown by an increase in both the peak growth rate and the unstable spectral bandwidth. Physically, both the spectral index and the nonextensive parameter act as control parameters for MI onset and analyzing the MI growth rate.

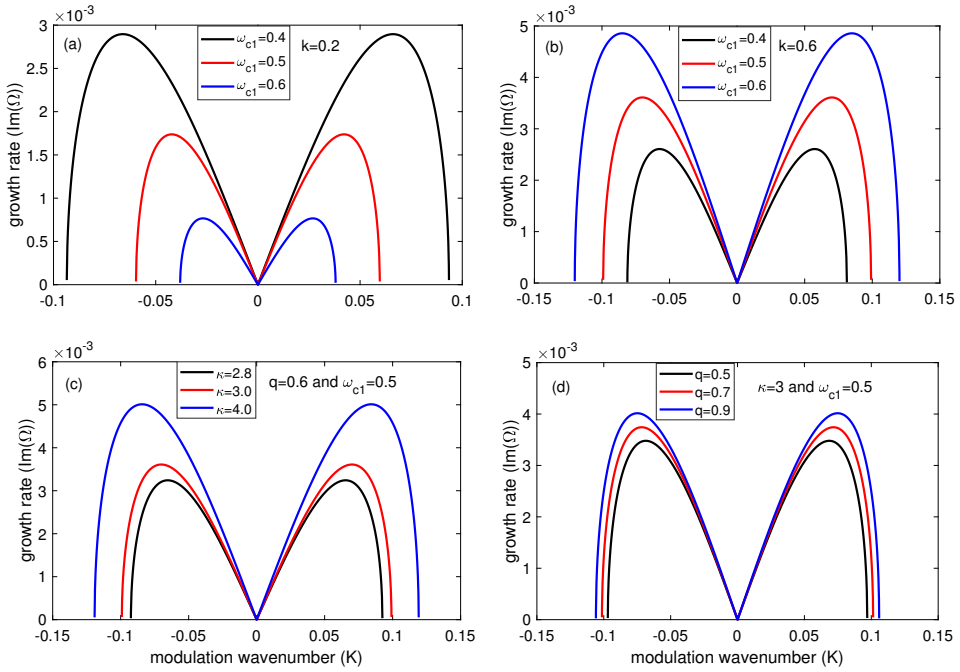


Figure 12. Variations in MI growth rate $\mathrm{Im}(\Omega)$, as a function of the modulation wavenumber K for magnetized HIAWs with $\omega_{c1} = 0.4$, 0.5, and 0.6 for (**a**) $k = 0.2$, (**b**) $k = 0.6$, (**c**) $\kappa = 2.8$, 3.0, and 4.0 at $q = 0.6$, and (**d**) $q = 0.5$, 0.7, and 0.9 at $\kappa = 3.0$. The fixed plasma parameters are $\Psi_0 = 0.1$, $\alpha = 0.5$, $\sigma = 0.5$, $\mu_e = 0.5$, $\mu_p = 0.3$, and $\alpha_e = 0.3$.

The impact of the electron population through the distribution function $\alpha_e = 0.3, 0.5, 0.7$ is shown in Figure 13a. Stronger electron contributions (α_e) physically enhance dispersive shielding, which reduces nonlinear self-focusing and suppresses the MI growth rate. The MI response approaches a weak growth rate where α_e slightly modify the instability profile, as evidenced by $\alpha_e = 0.5, 0.7$. We also examine the potential impact of the electron number density μ_e on the MI growth rate, as shown in Figure 13b; in this case, a significant and monotonic expansion in the unstable modulation region and an obvious increase in the growth rate with μ_e from 0.6 to 0.8. For the temperature ratio, we observe the similar trend of the MI growth rate as shown for the electron density ratio (see Figure 13c). The influence of the positron number density ratio (μ_p) on the MI growth rate is analyzed at fixed μ_e, as shown in Figure 13d. The instability bandwidth and peak growth rate are both enhanced by increasing μ_p. A larger population of positrons strengthens the modulational nonlinear interaction. As a result, instability is confined to a larger modulation domain, while the cutoff modulation wavenumber shifts toward lower K-limits. Higher electron concentration enhances the probability of envelope localization and develops more MI. The role of the electron species is asymmetrical when comparing the two figures directly: a rise in μ_p stabilizes the system by suppressing the growth rate, whereas an increase in μ_e destabilizes it by intensifying nonlinear coupling. The findings show that MI onset and the formation of nonlinear wave structures in magnetized multi-ion plasmas may be effectively controlled by modifying the ratios of ion to electron densities. The MI growth-rate spectrum exhibits the reflection of the MI growth rate about $K = 0$, satisfying $\mathrm{Im}(\Omega(K)) = \mathrm{Im}(\Omega(-K))$. Consequently, the negative modulation wavenumbers reproduce the same instability features as their positive counterparts, without introducing additional physical regimes. Both branches are presented in Figures 12 and 13 to explicitly demonstrate the even symmetry of the instability spectrum and its invariance under wavenumber reversal $K \to -K$.

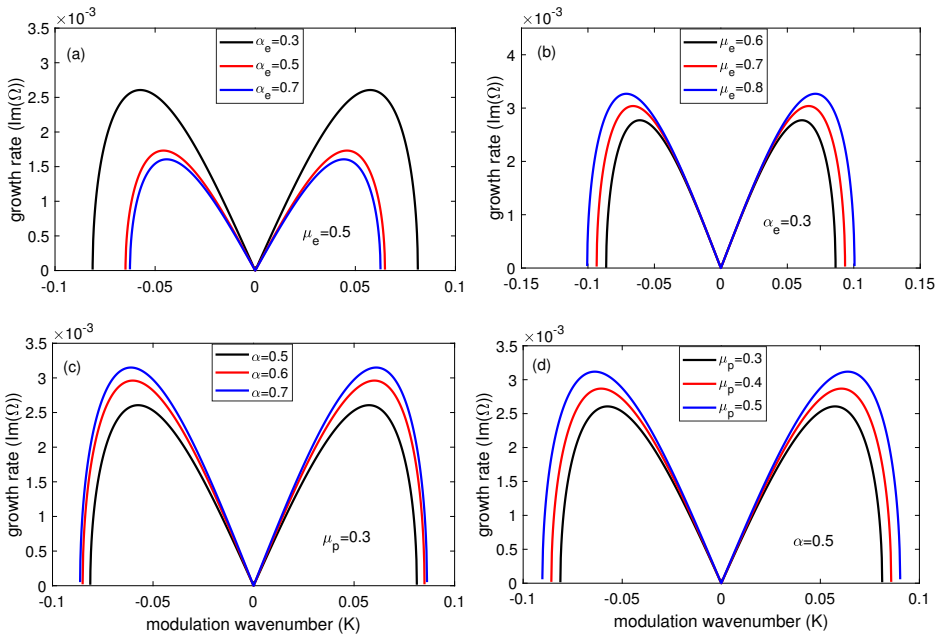


Figure 13. Variation in the MI growth rate, $\mathrm{Im}(\Omega)$, as a function of the modulation wavenumber K for magnetized HIAWs, showing the effects of (**a**) electron nonthermal parameter $\alpha_e = 0.3, 0.5, 0.7$ at $\mu_e = 0.5$, (**b**) electron concentration $\mu_e = 0.6, 0.7, 0.8$ at $\alpha_e = 0.3$, (**c**) effective ion mass ratio $\alpha = 0.5, 0.6, 0.7$ at $\mu_p = 0.3$, and (**d**) positron concentration $\mu_p = 0.3, 0.4, 0.5$ at $\alpha = 0.5$. The remaining parameters are fixed at $k = 0.6$, $\Psi_0 = 0.1$, $\sigma = 0.5$, $\omega_{c1} = 0.4$, $\kappa = 3$, while unspecified parameters retain the values $\alpha = 0.5$, $\alpha_e = 0.3$, $\mu_e = 0.5$, and $\mu_p = 0.3$.

6. Akhmediev Breathers

The nonlinear evolution of MI beyond its linear growth stage is described by the Akhmediev breather, which is an exact periodic solution of the NLSE. This phenomenon is usually called the Benjamin–Feir instability [59] in hydrodynamics and sideband instability [60] in nonlinear optics. Due to its general applicability, MI has been thoroughly studied in a variety of nonlinear systems, such as Bose–Einstein condensates [61] and plasma physics [62]. Physically, MI is defined as the concentration of wave energy into localized structures caused by the exponential amplification of weak sideband perturbations applied to a continuous-wave background. The NLSE [Equation (37)] yields the following precise Akhmediev breather solution under modulationally unstable conditions, that is, when the nonlinear and dispersive coefficients meet the criterion $PQ > 0$:

$$\Psi_{\mathrm{AB}}(\xi,\tau) = \left[\frac{\vartheta^3 \cosh\left(\frac{\sigma Q\tau}{2}\right) + i\vartheta\sigma \sinh\left(\frac{\sigma Q\tau}{2}\right)}{2\vartheta \cosh\left(\frac{\sigma Q\tau}{2}\right) - \sigma \cos\left(\vartheta\sqrt{\frac{Q}{2P}}\,\xi\right)} - 1\right] e^{iQ\tau}, \tag{45}$$

where $\sigma = \vartheta\sqrt{4-\vartheta^2}$ and the modulation parameter ϑ satisfies the condition $0 < \vartheta < 2$. The nonlinear evolution of magnetized HIAW envelopes in the unstable domain is described by the classical Akhmediev breather, which is equivalent to the above solution. It represents the periodic rise and decay of localized wave packets caused by MI because it is temporally localized in the evolution variable τ and spatially periodic in the propagation coordinate ξ.

The three-dimensional profiles of the Akhmediev breather solutions of magnetized HIAWs in the (ξ,τ) plane for numerous values of the modulation parameter ϑ are shown in Figure 14. The envelope amplitude of the breather is represented by the magnitude $|\Psi_{\mathrm{AB}}|$, which illustrates that the perturbation remains localized in the temporal coordinate (τ) while evolving continually in the spatial coordinate ξ. We observe the three localized

humps with peak amplitudes for $\vartheta = 0.6$ indicating the breather phenomenon as shown in Figure 14a. The periodic recurrence along ξ reflects the spatial periodicity of the Akhmediev breather solution and the localization in τ shows the concentration of HIAW energy in the form of isolated wave packets. In Figure 14b, as ϑ rises to 0.8, the Akhmediev breathers become closer to each other and may generate the two additional breathers in the same spatiotemporal domain $\xi \in [-40, 40]$. In addition, the number of breathers in the same spatial window grows and the peak amplitude increases at $\vartheta = 1.0$ [e.g., see Figure 14c]. This suggests that a higher modulation parameter amplifies MI which in turn generates the more energetic and frequent breathers. The system shows the highest degree of modulation as shown in Figure 14d for $\vartheta = 1.2$, with numerous peaks and same breather amplitude peaks. Higher ϑ-values strengthen the nonlinear self-modulation of magnetized HIAWs, supporting the formation of intense and short-lived wave packets that can evolve into extreme events, namely, rogue waves.

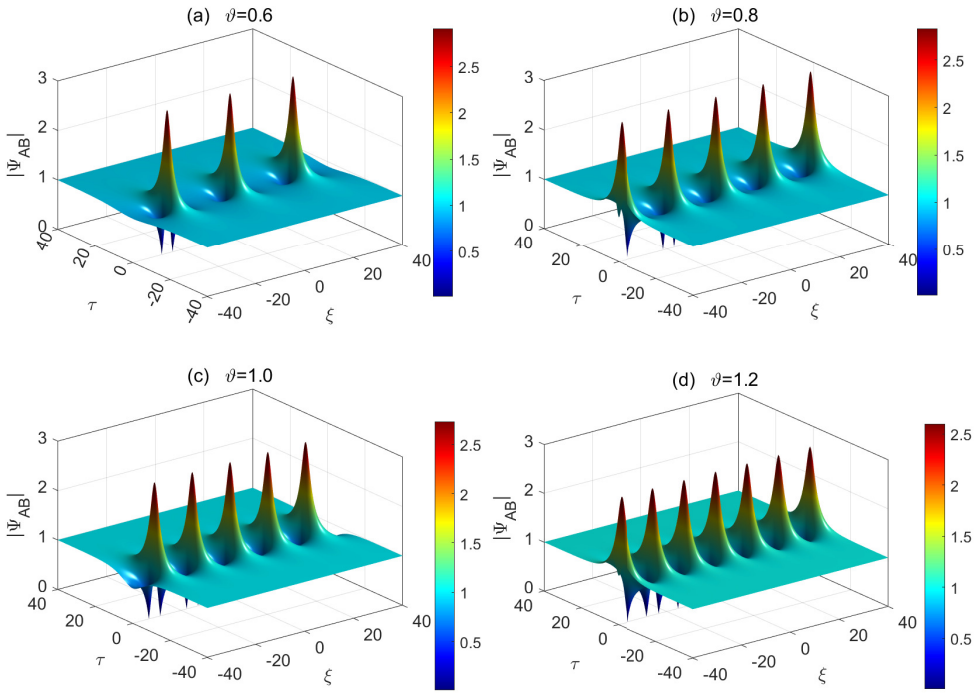


Figure 14. Surface profiles of the Akhmediev breather solutions for magnetized HIAWs with (**a**) $\vartheta = 0.6$, (**b**) $\vartheta = 0.8$, (**c**) $\vartheta = 1.0$, and (**d**) $\vartheta = 1.2$. Increasing the modulation parameter decreases the breather spacing while maintaining nearly the same maximum amplitude. The fixed parameters are $\alpha = 0.5$, $\sigma = 0.5$, $\omega_{c1} = 0.4$, $\mu_e = 0.5$, $\mu_p = 0.3$, $q = 0.6$, $\kappa = 3$, and $\alpha_e = 0.3$.

The contour plots depict the 2D distributions of the real and imaginary counterparts of the Akhmediev breathers in (ξ, τ)-plane under distinct values of the modulation parameter ϑ, as shown in Figure 15. The top row shows the amplitude of the real component and the bottom row shows its corresponding imaginary component of the breathers. The real component [see Figure 15a,b] shows a recurrence of envelope maxima that are periodically localized and centered around $\tau = 0$. The localized structures are widely spaced along the propagation direction for $\vartheta = 0.6$ [Figure 15a], suggesting a relatively weak modulation of the carrier wave. The number of localized peaks increases markedly as the modulation parameter rises to $\vartheta = 1.0$ [Figure 15b], indicating enhanced spatial localization of the breather structures. Simultaneously, the breather pattern exhibits stronger nonlinear self-focusing and increased spatial periodicity as the amplitude contrast between neighboring maxima and minima intensifies. The positive and negative lobes are shown symmetrically above and below the central axis in the imaginary part [see Figure 15c,d], which exhibits

an antisymmetric (dipolar) structure at $\tau = 0$. The dipolar structures are relatively broad with moderate amplitude, signifying a weaker phase modulation at $\varphi = 0.6$, as shown in Figure 15c. The strong modulation parameter $(\vartheta = 1.0)$ [see Figure 15d] results in more densely packed dipoles with significantly enhanced amplitudes, indicating stronger phase oscillations and better temporal localization of the breather dynamics.

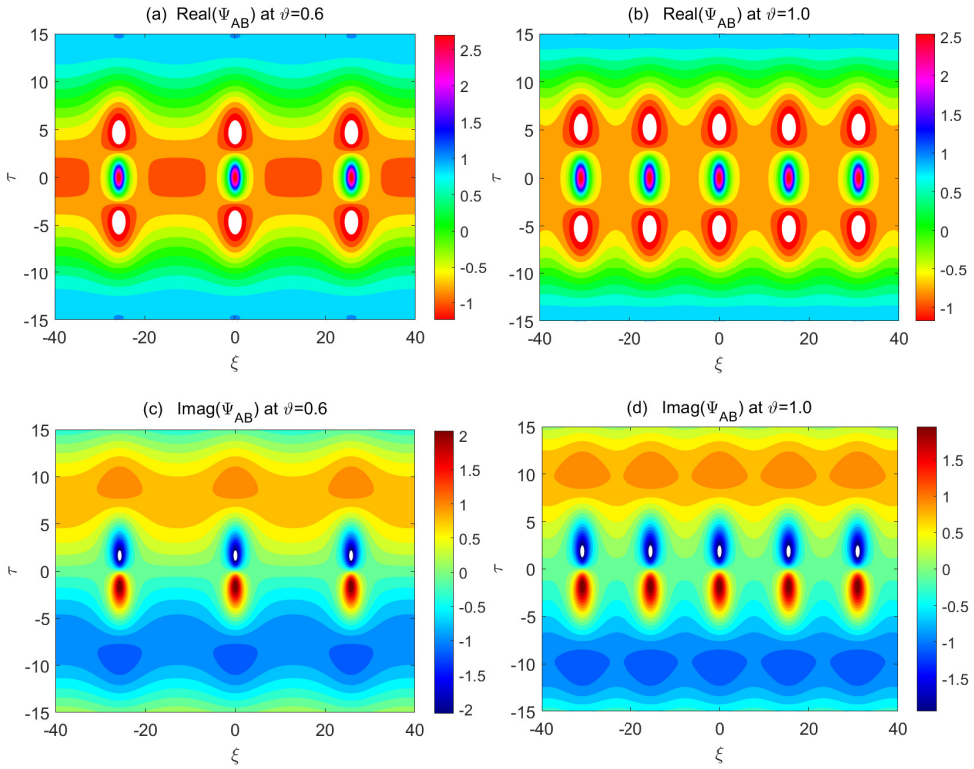


Figure 15. Contour plots of the Akhmediev breather (AB) solutions for magnetized HIAWs: (**a**,**b**) real component at $\nu = 0.6$ and 1.0, respectively, and (**c**,**d**) imaginary component at $\nu = 0.6$ and 1.0, respectively. Increasing the modulation parameter decreases the breather spacing and increases the spatial density of localized amplitude. The remaining plasma parameters are the same as those used in Figure 11.

The 1D profiles of the Akhmediev breather $|\Psi_{AB}|$ against spatial coordinate ξ for various plasma parameters are shown in Figure 16. The breather solutions at a fixed slow time τ show the spatial localization and periodicity of the envelope patterns, which are influenced by the modulation parameter (ϑ), magnetic field through ω_{c1}, and electron nonthermal population α_e. The impact of the modulation parameter is illustrated in Figure 16a,b. Three distinct localized peaks with equal amplitudes of the Akhmediev breather for $\vartheta = 0.6$ are observed [see Figure 16a], suggesting periodic localization along the propagation direction. The peak amplitude is found to be constant when the modulation parameter reaches to $\vartheta = 1.0$ [see Figure 16b], while significantly enhancing the number of breather peaks in the same spatial interval $\xi \in [-40, 40]$. This behavior suggests that the spatial modulation period is shortened by a higher modulation parameter, producing two more localized breathers without altering their maximum intensity. Figure 16c,d show the potential impact of the magnetic field. For weak magnetic field with $\omega_{c1} = 0.5$, five spatially periodic localized humps along ξ are observed, as shown in Figure 16c. Moreover, the number of breathers become closely spaced with strong magnetic field and may generate two additional polarity reversal peaks [see Figure 16d]. This suggests that the stronger magnetic field physically modifies the ratio of dispersion to nonlinearity, allowing more localized wave packets while maintaining the same peak amplitude. Figure 16e,f demonstrate the

impact of the electron nonthermal population α_e on the Akhmediev breather. The breathers are slightly more spaced in the same spatial domain with increasing electron population in the magnetized HIAW plasma. While first-order Akhmediev breathers describe fundamental modulation and localization processes, second-order breathers reveal richer nonlinear dynamics involving multiple interacting wave structures. Kedziora et al. [63] demonstrated that higher-order solutions can produce complex spatiotemporal localization and pronounced amplitude amplification. In the present magnetized plasma configuration, these features may be relevant to the formation of highly localized electrostatic wave packets and extreme nonlinear excitations.

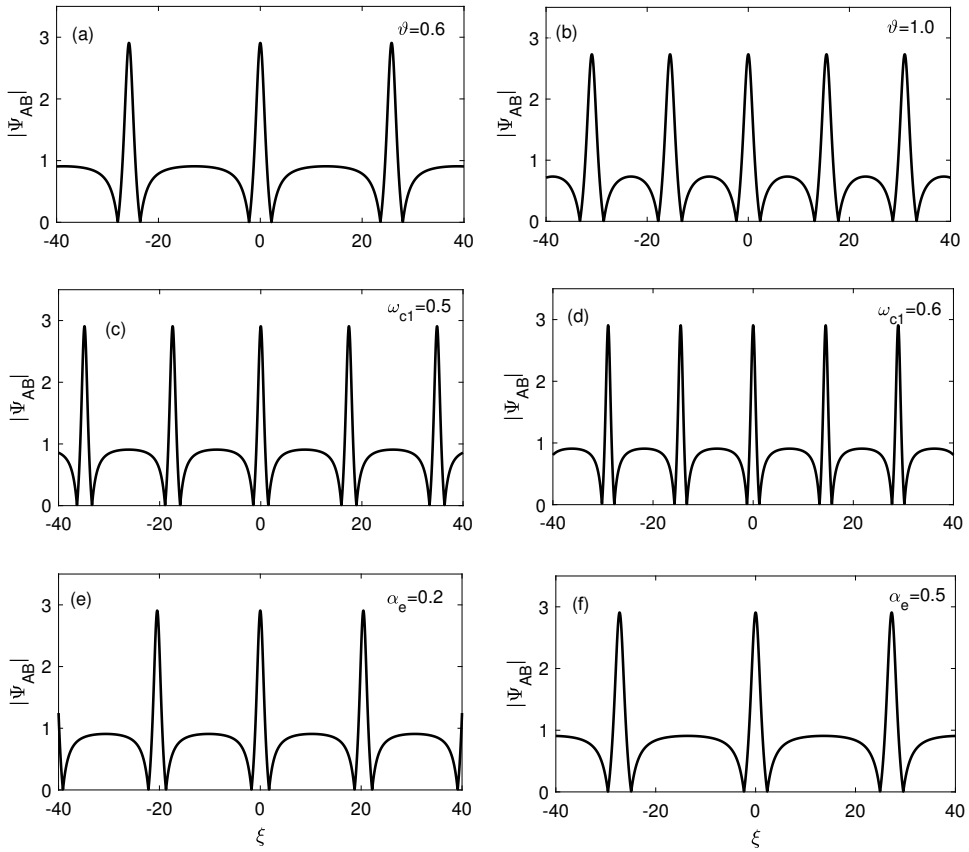


Figure 16. Spatial profiles of the Akhmediev breather amplitude $|\Psi_{AB}|$ for magnetized HIAWs: (**a**) $\vartheta = 0.6$ and (**b**) $\vartheta = 1.0$ at $\alpha = 0.5$, $\sigma = 0.5$, $\omega_{c1} = 0.4$, $\mu_e = 0.5$, $\mu_p = 0.3$, $q = 0.6$, $\kappa = 3$, and $\alpha_e = 0.3$; (**c**) $\omega_{c1} = 0.5$ and (**d**) $\omega_{c1} = 0.6$ at $\varphi = 0.6$; and (**e**) $\alpha_e = 0.2$ and (**f**) $\alpha_e = 0.5$ at $\omega_{c1} = 0.4$. Increasing ν and ω_{c1} decreases the breather spacing, whereas increasing α_e enlarges the spatial period.

7. Conclusions

To summarize, this study develops a unified framework for describing nonlinear wave dynamics and modulational instability (MI) in magnetized heavy ion-acoustic plasmas. Starting from the magnetized heavy ion-acoustic model, the nonlinear wave dynamics are described by an NLSE, derived using the reductive perturbation scheme and subsequently transformed into a planar Hamiltonian system through a traveling-wave transformation. The phase-space analysis reveals the coexistence of NPTs, NHTs, and SPTs with homoclinic separatrices that establish transitions between different nonlinear wave states. The associated analytical solutions confirm the existence of both compressive and rarefactive solitary waves. Polarity reversal results in mirror-symmetric wave patterns, revealing the intrinsic symmetry of the conservative Hamiltonian system. Furthermore, increasing ω_{c1}, κ, q, and carrier wavenumber (k) reduces the amplitudes of both solitary-wave polarities. The principal contributions of the present investigation lie in elucidating the influence

of external magnetization on Hamiltonian phase-space dynamics, modulational stability, and Akhmediev breather evolution in non-Maxwellian heavy ion-acoustic plasmas. The results demonstrate that increasing magnetic-field strength modifies the spatial extent of Hamiltonian trajectories while preserving their characteristic topology, with symmetric homoclinic orbits supporting paired compressive and rarefactive solitary-wave structures. Furthermore, two disconnected modulationally stable regions separated by an unstable domain are identified, whose characteristics are significantly influenced by magnetic-field strength and plasma parameters. The derived cubic NLSE governs the slow modulation of finite-amplitude HIAW packets and provides the basis for examining MI, envelope solitons, chaotic dynamics, and Akhmediev breather excitations. The two stable regions support dark envelope solitons, whereas the unstable region admits bright envelope solitons alongside the onset of MI. Unlike conventional plasma systems exhibiting a single stability transition, the present Kappa-Cairns–Tsallis plasma configuration supports two distinct dark-soliton regimes, highlighting the role of combined non-Maxwellian electron and positron distributions in governing the stability–instability transition. The analysis also reveals that magnetization modifies the spatial periodicity and localization characteristics of Akhmediev breathers. Collectively, these findings establish a unified connection between Hamiltonian dynamics, modulational instability, and nonlinear breather excitations, highlighting the role of magnetization in controlling nonlinear wave behavior in non-Maxwellian plasmas.

The present findings are broadly consistent with previous investigations of nonlinear wave propagation in magnetized electron–positron–ion plasmas, while offering further insight into the underlying nonlinear dynamics. Mahmood et al. [46] demonstrated the influence of positron concentration and plasma composition on ion–acoustic solitary waves, whereas Alinejad et al. [47] emphasized the role of suprathermal electrons in modifying wave propagation. Similarly, Chowdhury et al.[10] explored modulational instability and rogue-wave formation in unmagnetized multi-ion plasmas, while Bacha et al. [48] investigated ion-acoustic wave dynamics in magnetized plasma environments. Building on these studies, the present work examines the combined effects of κ-Cairns-distributed electrons, nonextensive positrons, and external magnetic fields on the nonlinear behavior of heavy ion-acoustic waves. A key finding is the emergence of two disconnected modulationally stable regions separated by an unstable domain, together with polarity-reversal-symmetric solitary waves and exact Akhmediev breather solutions. Our analysis further reveals that magnetic-field strength influences the spatial extent of Hamiltonian trajectories and breather spacing, while non-Maxwellian plasma parameters modify solitary-wave amplitudes and instability characteristics. These results provide a more comprehensive picture of how plasma composition and magnetic fields govern nonlinear wave stability, localization, and energy concentration, with potential relevance to coherent electrostatic structures observed in Earth's magnetosphere, astrophysical environments, and laboratory multi-ion plasmas.

The impact of the magnetic field, effective ion mass ratio, κ-Cairns spectral parameters and the Tsallis nonextensive index on the MI onset, instability growth rate, and its bandwidth has been analyzed systematically. Moreover, we have examined the nonlinear evolution of localized wave packets through exact Akhmediev breather solutions of the NLSE. The breather dynamics demonstrate the periodic amplification and localization of wave envelopes prior to their decay back into the continuous background, confirming the development of MI in the unstable domain. In addition, the chaotic evolution of the envelope dynamics has been examined for both dark- and bright-soliton regimes. These findings may provide useful physical prospects into nonlinear electrostatic wave phenomena occurring in astrophysical and space plasmas, including planetary magnetospheres, pulsar environments, the Earth's ionosphere, and laboratory magnetized plasma devices,

where non-Maxwellian particle populations are usually observed. Future studies involving direct numerical simulations of the four-component plasma fluid model could further clarify the stability, robustness, and nonlinear evolution of the derived solitary-wave and breather solutions. Such investigations, together with higher-order nonlinear models and multidimensional extensions, represent promising directions for future research. The present analysis neglects electron–positron annihilation processes and assumes that the characteristic timescale of nonlinear wave evolution is considerably shorter than the annihilation timescale. Future investigations will incorporate annihilation effects to evaluate their influence on plasma equilibrium, MI, and nonlinear wave.

Author Contributions: A.K.: Conceptualization, writing—original draft, investigation, software; Y.Y.: Writing—review and editing, validation, formal analysis; W.A.: Visualization, conceptualization, formal analysis, writing—review and editing; Y.J.: Validation, methodology, data curation, visualization; G.Y.: Visualization, validation, formal analysis, supervision; T.R.: Conceptualization, writing—review and editing, visualization, validation. All authors have read and agreed to the published version of the manuscript.

Funding: The APC was funded by Qassim University (QU-APC-2026).

Institutional Review Board Statement: Not applicable.

Informed Consent Statement: Not applicable.

Data Availability Statement: The data that support the findings of this study are available from the corresponding authors upon reasonable request.

Acknowledgments: The Researchers would like to thank the Deanship of Graduate Studies and Scientific Research at Qassim University (https://www.qu.edu.sa) for financial support (QU-APC-2026). The authors extend their appreciation to the Deanship of Scientific Research, Islamic University of Madinah, Saudi Arabia, for funding this research work.

Conflicts of Interest: The authors declare no conflict of interest.

References

1. Shatashvili, N.L.; Javakhishvili, J.I.; Kaya, H. Nonlinear wave dynamics in two-temperature electron-positron-ion plasma. *Astrophys. Space Sci.* **1997**, *250*, 109–115.
2. Jannat, S.; Chowdhury, N.A.; Mannan, A.; Mamun, A.A. Ion-acoustic rogue waves in a multi-component plasma medium. *Chin. J. Phys.* **2022**, *77*, 2228–2237.
3. Rehman, M.A.; Mishra, M.K. Ion-acoustic Gardner Solitons in electron-positron-ion plasma with two-electron temperature distributions. *Phys. Plasmas* **2016**, *23*.
4. Thorne, K.S.; Misner, C.W.; Wheeler, J.A. *Gravitation*; Freeman: San Francisco, CA, USA, 2000.
5. Michel, F.C. Theory of pulsar magnetospheres. *Rev. Mod. Phys.* **1982**, *54*, 1.
6. Michel, F.C. *Theory of Neutron Star Magnetospheres*; University of Chicago Press: Chicago, IL, USA, 1991.
7. Shukla, P.K.; Yu, M.Y.; Tsintsadze, N.L. Intense solitary laser pulse propagation in a plasma. *Phys. Fluids* **1984**, *27*, 327–328.
8. Shukla, P.K.; Rao, N.N.; Yu, M.Y.; Tsintsadze, N.L. Relativistic nonlinear effects in plasmas. *Phys. Rep.* **1986**, *138*, 1–149.
9. Surko, C.M.; Murphy, T.J. Use of the positron as a plasma particle. *Phys. Fluids B* **1990**, *2*, 1372–1375.
10. Chowdhury, N.A.; Mannan, A.; Hasan, M.M.; Mamun, A.A. Heavy ion-acoustic rogue waves in electron-positron multi-ion plasmas. *Chaos* **2017**, *27*, 093105.
11. Kourakis, I.; Shukla, P.K. Ion-acoustic waves in a two-electron-temperature plasma: Oblique modulation and envelope excitations. *J. Phys. A Math. Gen.* **2003**, *36*, 11901–11913.
12. Alinejad, H.; Mahdavi, M.; Shahmansouri, M. Modulational instability of ion-acoustic waves in a plasma with two-temperature kappa-distributed electrons. *Astrophys. Space Sci.* **2014**, *352*, 571–578.
13. Bouzit, O.; Tribeche, M. Dust-acoustic waves modulational instability and rogue waves in a polarized dusty plasma. *Phys. Plasmas* **2015**, *22*, 103703.
14. Douanla, D.V.; Tiofack, C.G.A.; Mohamadou, A. Heavy ion–acoustic rogue waves in magnetized electron–positron multi-ion plasmas. *Contrib. Plasma Phys.* **2020**, *60*, e202000036.

15. Chowdhury, N.A.; Hasan, M.M.; Mannan, A.; Mamun, A.A. Nucleus-acoustic envelope solitons and their modulational instability in a degenerate quantum plasma system. *Vacuum* **2018**, *147*, 31–37.
16. Khan, A.; Farooq, A.; Shaaban, S.M.; Hafiz, A. Role of modified Cairns–Tsallis distribution on modulational instability and Akhmediev breathers in electronegative plasmas. *Commun. Nonlinear Sci. Numer. Simul.* **2025**, *150*, 108967.
17. Abdelwahed, H.G.; El-Shewy, E.K.; Zahran, M.A.; Elwakil, S.A. On the rogue wave propagation in ion pair superthermal plasma. *Phys. Plasmas* **2016**, *23*. https://doi.org/10.1063/1.4940679.
18. Khan, A.; Farooq, A.; Abid, A.A.; Hussain, M.S.; Ma, W.X.; Shaaban, S.M. Exploring non-Maxwellian distributions effects on modulational instability and rogue wave triplets in ion-acoustic plasmas. *Chaos Solitons Fractals* **2025**, *195*, 116262.
19. Haque, M.N.; Mannan, A. Dynamics of ion-acoustic rogue waves in electron-positron-ion magneto-plasmas. *Contrib. Plasma Phys.* **2021**, *61*, e202000161.
20. Kharif, C.; Pelinovsky, E.; Slunyaev, A. *Rogue Waves in the Ocean*; Springer Science & Business Media: Berlin/Heidelberg, Germany, 2008.
21. Shats, M.; Punzmann, H.; Xia, H. Capillary rogue waves. *Phys. Rev. Lett.* **2010**, *104*, 104503.
22. Bailung, H.; Sharma, S.K.; Nakamura, Y. Observation of Peregrine solitons in a multicomponent plasma with negative ions. *Phys. Rev. Lett.* **2011**, *107*, 255005.
23. Chabchoub, A.; Hoffmann, N.P.; Akhmediev, N. Rogue wave observation in a water wave tank. *Phys. Rev. Lett.* **2011**, *106*, 204502.
24. Kibler, B.; Fatome, J.; Finot, C.; Millot, G.; Dias, F.; Genty, G.; Akhmediev, N.; Dudley, J.M. The Peregrine soliton in nonlinear fibre optics. *Nat. Phys.* **2010**, *6*, 790–795.
25. Bludov, Y.V.; Konotop, V.V.; Akhmediev, N. Matter rogue waves. *Phys. Rev. A* **2009**, *80*, 033610.
26. El-Labany, S.K.; Moslem, W.M.; El-Bedwehy, N.A.; Sabry, R.; Abd El-Razek, H.N. Rogue wave in Titan's atmosphere. *Astrophys. Space Sci.* **2012**, *338*, 3–8.
27. Sabry, R.; Moslem, W.M.; Shukla, P.K. Freak waves in white dwarfs and magnetars. *Phys. Plasmas* **2012**, *19*. https://doi.org/10.1063/1.4772058.
28. Wang, D.; Liu, Z.; Zhao, H.; Qin, H.; Bai, G.; Chen, C.; Shi, P.; Du, Y.; Zhao, Y.; LIu, W.; et al. Launching by cavitation. *Science* **2025**, *389*, 935–939.
29. Jia, Y.-H.; Wang, D.-L.; Shen, B.; Ju, Z.-T.; Huang, Q.-Y.; Wang, X.-P.; Zhang, J.-H.; Wang, Y.-Y.; Liu, W.; Dai, C.-Q. Predicting Ultrafast Soliton Evolution via a Parameter-Driven Neural Network. *Laser Photonics Rev.* **2026**, e03212.
30. Ahmad, M.; Shahzad, M.A. Revisiting some analytical and numerical interpretations of Cairns and Kappa–Cairns distribution functions. *Phys. Plasmas* **2020**, *27*, 100901.
31. Djebli, M.; Marif, H. Large amplitude double layers in a positively charged dusty plasma with nonthermal electrons. *Phys. Plasmas* **2009**, *16*, 063708 .
32. Cairns, R.A.; Mamum, A.A.; Bingham, R.; Boström, R.; Dendy, R.O.; Nairn, C.M.C.; Shukla, P.K. Electrostatic solitary structures in non-thermal plasmas. *Geophys. Res. Lett.* **1995**, *22*, 2709–2712. Correction in *Geophys. Res. Lett.* **2011**, *38*, L13309.
33. Livadiotis, K.D. *Theory and Applications in Plasmas*; Elsevier: Amsterdam, The Netherlands, 2016.
34. Burlaga, L.F. Heliospheric magnetic fields and plasmas. *Rev. Geophys.* **1983**, *21*, 363–375.
35. Vasyliunas, V.M. A survey of low-energy electrons in the evening sector of the magnetosphere with OGO 1 and OGO 3. *J. Geophys. Res.* **1968**, *73*, 2839–2884.
36. Mace, R.L.; Hellberg, M.A. A dispersion function for plasmas containing superthermal particles. *Phys. Plasmas* **1995**, *2*, 2098–2109.
37. Debnath, D.; Bandyopadhyay, A. Combined effect of Kappa and Cairns distributed electrons on ion acoustic solitary structures in a collisionless magnetized dusty plasma. *Astrophys. Space Sci.* **2020**, *365*, 72.
38. Saini, N.S.; Kourakis, I.; Hellberg, M.A. Arbitrary amplitude ion-acoustic solitary excitations in the presence of excess superthermal electrons. *Phys. Plasmas* **2009**, *16*, 062903.
39. El-Tantawy, S.A.; El-Bedwehy, N.A.; Moslem, W.M. Nonlinear ion-acoustic structures in dusty plasma with superthermal electrons and positrons. *Phys. Plasmas* **2011**, *18*, 052113.
40. Kourakis, I.; Sultana, S.; Hellberg, M.A. Dynamical characteristics of solitary waves, shocks and envelope modes in kappa-distributed non-thermal plasmas: An overview. *Plasma Phys. Control. Fusion* **2012**, *54*, 124001.
41. Mamun, A.A.; Cairns, R.A. Stability of solitary waves in a magnetized non-thermal plasma. *J. Plasma Phys.* **1996**, *56*, 175–185.
42. Pillay, S.R.; Verheest, F. Effect of non-thermal ion distributions on the Jeans instability in dusty plasmas. *J. Plasma Phys.* **2005**, *71*, 177–184.
43. Verheest, F.; Hellberg, M.A.; Baluku, T.K. Arbitrary amplitude ion-acoustic soliton coexistence and polarity in a plasma with two ion species. *Phys. Plasmas* **2012**, *19*, 032305.
44. Debnath, D.; Bandyopadhyay, A.; Das, K.P. Ion acoustic solitary structures in a magnetized nonthermal dusty plasma. *Phys. Plasmas* **2018**, *25*, 033704.
45. Aoutou, K.; Tribeche, M.; Zerguini, T.H. Electrostatic solitary structures in dusty plasmas with nonthermal and superthermal electrons. *Phys. Plasmas* **2008**, *15*, 013702.

46. Mahmood, S.; A, M.; Saleem, H. Ion acoustic solitary wave in homogeneous magnetized electron-positron-ion plasmas. *New J. Phys.* **2003**, *5*, 28.
47. Alinejad, H.; Mamun, A.A. Oblique propagation of electrostatic waves in a magnetized electron-positron-ion plasma with superthermal electrons. *Phys. Plasmas* **2011**, *18*, 112103.
48. Bacha, M.; Ait Gougam, L.; Tribeche, M. Ion-acoustic rogue waves in magnetized solar wind plasma with nonextensive electrons. *Physica A* **2017**, *466*, 199–210.
49. Khan, A.; Awaji, M.Y.; Shaaban, S.M.; Hafiz, P.A.; Ahmad, N.; Abid, A.A.; Guangrui, Y. Signature of second stable regime of modulational instability and rogue wave triplets in dual-polarity dusty plasmas. *Phys. Rev. E* **2025**, *112*, 065202.
50. Hellberg, M.A.; Mace, R.L. Generalized plasma dispersion function for a plasma with a kappa-Maxwellian velocity distribution. *Phys. Plasmas* **2002**, *9*, 1495–1504.
51. Hellberg, M.A.; Mace, R.L.; Baluku, T.K.; Kourakis, I.; Saini, N.S. Comment on "Mathematical and physical aspects of Kappa velocity distribution" [Phys. Plasmas 14, 110702 (2007)]. *Phys. Plasmas* **2009**, *16*, 094701.
52. Podesta, J.J. Spatial Landau damping in plasmas with three-dimensional κ distributions. *Phys. Plasmas* **2005**, *12*, 052101.
53. Dovner, P.O.; Eriksson, A.I.; Boström, R.; Holback, B. Freja multiprobe observations of electrostatic solitary structures. *Geophys. Res. Lett.* **1994**, *21*, 1827–1830.
54. Verheest, F.; Pillay, S.R. Large amplitude dust-acoustic solitary waves and double layers in nonthermal plasmas. *Phys. Plasmas* **2008**, *15*.
55. Pierrard, V.; Lazar, M. Kappa distributions: Theory and applications in space plasmas. *Sol. Phys.* **2010**, *267*, 153–174.
56. Livadiotis, G.; McComas, D.J. Understanding kappa distributions: A toolbox for space science and astrophysics. *Space Sci. Rev.* **2013**, *175*, 183–214. Correction in *Space Sci. Rev.* **2013**, *175*, 215.
57. Panguetna, C.S.; Tabi, C.B.; Kofané, T.C. Electronegative nonlinear oscillating modes in plasmas. *Commun. Nonlinear Sci. Numer. Simul.* **2018**, *55*, 326–337.
58. Khan, A.; Abid, A.A.; Khan, M.; Kengne, E. Quantifying the effects of generalized (r, q) distribution function on modulational instability and rogue wave of electron acoustic solitons. *Phys. Scr.* **2025**, *100*, 065204.
59. Benjamin, T.B.; Feir, J.E. The disintegration of wave trains on deep water Part 1. Theory. *J. Fluid Mech.* **1967**, *27*, 417–430.
60. Ostrovskii, L.A. Propagation of wave packets and space-time self-focusing in a nonlinear medium. *Sov. Phys. JETP* **1967**, *24*, 797–800.
61. Konotop, V.V.; Salerno, M. Modulational instability in Bose-Einstein condensates in optical lattices. *Phys. Rev. A* **2002**, *65*, 021602.
62. Taniuti, T.; Washimi, H. Self-trapping and instability of hydromagnetic waves along the magnetic field in a cold plasma. *Phys. Rev. Lett.* **1968**, *21*, 209.
63. Kedziora, D.J.; Ankiewicz, A.; Akhmediev, N. Circular rogue wave clusters. *Phys. Rev. E* **2011**, *84*, 056611.

Disclaimer/Publisher's Note: The statements, opinions and data contained in all publications are solely those of the individual author(s) and contributor(s) and not of MDPI and/or the editor(s). MDPI and/or the editor(s) disclaim responsibility for any injury to people or property resulting from any ideas, methods, instructions or products referred to in the content.